




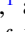



Spin dynamics of charged excitons in ultrathin (In,Al)(Sb,As)/AlAs and Al(Sb,As)/AlAs quantum wells with an indirect band gap

T. S. Shamirzaev ¹, D. R. Yakovlev ^{1,2,3}, N. E. Kopteva ², D. Kudlacik ², M. M. Glazov ³, A. G. Krechetov,⁴
A. K. Gutakovskii ¹ and M. Bayer ^{2,3}

¹*Rzhanov Institute of Semiconductor Physics, Siberian Branch of the Russian Academy of Sciences, 630090 Novosibirsk, Russia*

²*Experimentelle Physik 2, Technische Universität Dortmund, 44227 Dortmund, Germany*

³*Ioffe Institute, Russian Academy of Sciences, 194021 St. Petersburg, Russia*

⁴*Kemerovo State University, 650000 Kemerovo, Russia*



(Received 23 May 2022; revised 21 July 2022; accepted 22 July 2022; published 9 August 2022)

The charged exciton recombination and their spin dynamics are studied in ultrathin InSb- and AlSb-based quantum wells (QWs) surrounded by an AlAs matrix characterized by an indirect band gap. Strong material intermixing was observed that results in the QWs being composed of a quaternary $\text{In}_x\text{Al}_{1-x}\text{Sb}_y\text{As}_{1-y}$ or a ternary $\text{AlSb}_y\text{As}_{1-y}$ alloy. The band alignment in these QWs is identified as type I for (In,Al)(Sb,As)/AlAs and type II for Al(Sb,As)/AlAs. The magnetic-field-induced circular polarization of the photoluminescence P_c is studied as function of the field strength. The observed nonmonotonic behavior of the P_c dynamics at high magnetic fields is provided by the interplay of negative and positive trions, contributing to the emission. To interpret the experiment, we have developed a kinetic equation model which accounts for the dynamics of the trion spin states and the redistribution of trions between these states as a result of spin relaxation. The model is in quantitative agreement with the experiment and allows us to determine trion radiative lifetimes on the order of hundreds of microseconds, holes in the trion spin-relaxation times also in the hundreds of μs range, electrons in the trion spin-relaxation times of hundreds of ns, and heavy-hole g factors of about $+3.5$ for the structures studied.

DOI: [10.1103/PhysRevB.106.075407](https://doi.org/10.1103/PhysRevB.106.075407)

I. INTRODUCTION

Heterostructures with semiconductor quantum wells (QWs) are interesting from several points of view, including basic physics as well as optoelectronic and spintronic applications [1–9]. Among the different types of QWs, the longest exciton lifetimes up to milliseconds are obtained in indirect band-gap heterostructures. These long times are owing to the separation in the momentum space of the oppositely charged carriers that form the excitons [10–12]. Since the spin-relaxation time of localized electrons can reach milliseconds due to suppression of spin-orbit coupling effects, as shown theoretically and experimentally [13–15], QWs with indirect band gap are highly interesting for studying long-lived localized exciton spin dynamics, which are not limited by exciton recombination [16–19]. A convenient technique to address the dynamics of electron and exciton spins localized in QWs is to track the redistribution of populations between the spin states split by a magnetic field, which manifests itself in the magnetically induced circular polarization [20]. The redistribution of exciton populations between optically bright and dark states leads to a circular polarization of the photoluminescence (PL) induced by the magnetic field. It was experimentally demonstrated recently in thin QWs with an indirect band gap of type-II (GaAs/AlAs [21–23]) and type-I ((In,Al)As/AlAs [24]) band alignment. Both types of QWs have shown a high degree of circular polarization in magnetic field, which is related

to (i) long exciton lifetimes, which markedly exceed the spin-relaxation times of electrons and holes, and (ii) large g -factor values of the charge carriers. However, a surprisingly low circular polarization degree (almost zero) of the magnetic-field-induced PL was observed recently in Ref. [25] for an antimony-based thin indirect band gap (Ga,Al)(Sb,As)/AlAs QWs with long PL lifetime that strongly exceeds the carrier spin-relaxation times, as well as with electron and hole g factors similar to those in GaAs/AlAs QWs [22].

In this paper, we investigate the effect of a magnetic field on the recombination and spin dynamics of charge carriers in ultrathin antimony-based indirect band gap QWs with band alignment of type-I for (In,Al)(Sb,As)/AlAs and of type-II for Al(Sb,As)/AlAs. We demonstrate that in contrast to previously studied ultrathin indirect band gap GaAs/AlAs and (In,Al)As/AlAs QWs, where the spin and recombination dynamics of photoexcited charge carriers are determined by the distribution over exciton bright and dark states [21,22,24,26], the ultrathin antimony-based (In,Al)(Sb,As)/AlAs and Al(Sb,As)/AlAs QWs with a similar energy spectrum show qualitatively different spin and recombination dynamics of the charge carriers. Surprisingly, the PL intensity of the QWs studied in this paper does not change in magnetic field. Furthermore, the dynamics of the PL circular polarization degree (P_c) are unusually nonmonotonic. The P_c rises for several tens of microseconds, reaches a maximal value, and then decreases on longer timescales. This unexpected experimental behavior is explained by a the-

oretical model taking into account the spatial separation of electrons and holes localized on fluctuations of the QW interfaces. The carrier separation results in formation of negatively and positively charged excitons (trions) that recombine in a magnetic field, leading to emission of σ^- and σ^+ circularly polarized photons, respectively. As a result, the dynamics of the PL circular polarization are nonmonotonic and the time-integrated polarization of the emission is close to zero.

The paper is organized as follows. In Sec. II, the studied samples and the experimental techniques are described. In Sec. III, we present the experimental data from transmission electron microscopy and also on the exciton dynamics obtained in an external magnetic field by time-integrated and time-resolved PL. Also, the time-integrated and time-resolved circular polarization of the PL induced by the magnetic field are given. The theoretical model describing the negative and positive trion dynamics in the ultrathin QWs is presented in Sec. IV. The experimental data are analyzed in the frame of this model. We also perform model calculations for several cases of interest for future experimental studies (Sec. V). The conclusion is given in Sec. VI.

II. EXPERIMENTAL DETAILS

The (In,Al)(Sb,As)/AlAs and Al(Sb,As)/AlAs ultrathin QWs studied in this paper were grown by molecular-beam epitaxy on semi-insulating (001)-oriented GaAs substrates in a Riber Compact system. The structures consist of a layer with a nominal thickness of 0.25 monolayers (MLs) of InSb or AlSb embedded between 50-nm-thick layers of AlAs, grown on top of a 200-nm-thick GaAs buffer layer. The lower AlAs layer in all structures was grown at a temperature of 620 °C. Then the growth was interrupted, and the substrate temperature was decreased down to 480 °C under As flux during cooling. The AlAs surface has a $c(4 \times 4)$ reconstruction (measured by the reflection high-energy electron diffraction technique). The InSb or AlSb layers were deposited at a rate of 0.1 ML/s as calibrated in the center of the wafer using reference samples. The accuracy of the material deposition was better than 0.05 ML. The upper AlAs layer was grown at the same substrate temperature as the corresponding InSb or AlSb layers. A 20-nm-thick GaAs cap layer protects the top AlAs layer against oxidation.

The atomic structure of the samples was analyzed by scanning transmission electron microscopy (STEM) employing a Titan 80-300 FEI device. Visualization of the distribution of chemical elements (chemical mapping) was performed using energy dispersive X-ray spectroscopy (EDAX) with a spatial resolution of 1 nm.

The samples were placed in a split-coil magnet cryostat and exposed to magnetic fields up to $B = 8$ T. The angle θ between the magnetic field direction and the QW growth axis (z axis) was varied between 0° (Faraday geometry) and 45° . The temperature was varied from $T = 1.6$ K up to 60 K. The time-resolved and time-integrated PL was excited by the third harmonic of a Q-switched Nd:YVO₄ laser (3.49 eV) with a pulse duration of 5 ns. The pulse energy density was kept below 100 nJ/cm² and the pulse-repetition frequency could be varied from 400 Hz up to 100 kHz [27]. Steady-state PL was

excited by a semiconductor laser diode with photon energy of 3.07 eV and excitation density that could cover the range from 1 mW/cm² to 30 W/cm² by using a gradient neutral filter. The emitted light was dispersed by a 0.5-m monochromator. For the time-integrated measurements, the PL was detected by a liquid-nitrogen-cooled charge-coupled-device camera, while for the time-resolved measurements a GaAs photomultiplier combined with a time-correlated photon-counting module was used. To monitor the PL decay in a wide temporal range up to 2.5 ms, the time resolution of the detection system (i.e., the binning range of the photon counting events) was varied between 32 ns and 2.5 μ s.

The exciton spin dynamics were analyzed from the PL by measuring the circular polarization degree P_c induced by the external magnetic field. P_c was evaluated from the data by

$$P_c = \frac{I_{\sigma^+} - I_{\sigma^-}}{I_{\sigma^+} + I_{\sigma^-}},$$

where I_{σ^+} and I_{σ^-} are the intensities of the σ^+ and σ^- polarized PL components, respectively. To determine the sign of P_c , we performed a control measurement on a diluted magnetic semiconductor structure with (Zn,Mn)Se/(Zn,Be)Se QWs for which $P_c > 0$ in Faraday geometry [28].

III. EXPERIMENTAL RESULTS

A. Transmission electron microscopy

A cross-section TEM image and chemical mapping of Al, In, Ga, As, and Sb in cross-section STEM images for the Al(Sb,As)/AlAs and (In,Al)(Sb,As)/AlAs as well as the recently studied [25] (Ga,Al)(Sb,As)/AlAs heterostructures containing QWs with a nominal thickness of 0.25 ML are shown in Fig. 1.

Let us take a closer look at these chemical maps. The thickness of the QW, which was estimated from the Ga, In, or Sb atom spread, exceeds the nominal one ML according to the design of the growth procedure for all studied structures. Therefore, material intermixing occurs and the QWs contain either a ternary AlSb_yAs_{1-y} alloy or a quaternary In_xAl_{1-x}Sb_yAs_{1-y}, respectively Ga_xAl_{1-x}Sb_yAs_{1-y} alloy. One can see that the profile of the material spread strongly depends on the chemical elements forming the QW.

Commonly, thin QWs such as, for example, GaAs/AlAs [21] or InAs/InP [29] were described as thin slabs with abrupt heterointerfaces. However, microscopy shows that a strong intermixing of the well and barrier materials takes place for In and Sb containing layers placed in a AlAs matrices. This intermixing occurs due to strain-driven segregation [30–36]. Thus, the indium and antimony composition profiles across a QW are not abrupt. To describe the material profile in the case of one component segregation, such as, for example, in structures combining InAs/AlAs or AlSb/AlAs heteropairs, the phenomenological model of Muraki *et al.* [37] can be used [18,31]. In the framework of this model, the indium (antimony) composition x along the QW growth direction is described as [37]

$$\begin{aligned} x(n) &= x_0(1 - R^n), \quad 1 \leq n \leq N, \\ x(n) &= x_0(1 - R^N)R^{n-N}, \quad n > N. \end{aligned} \quad (1)$$

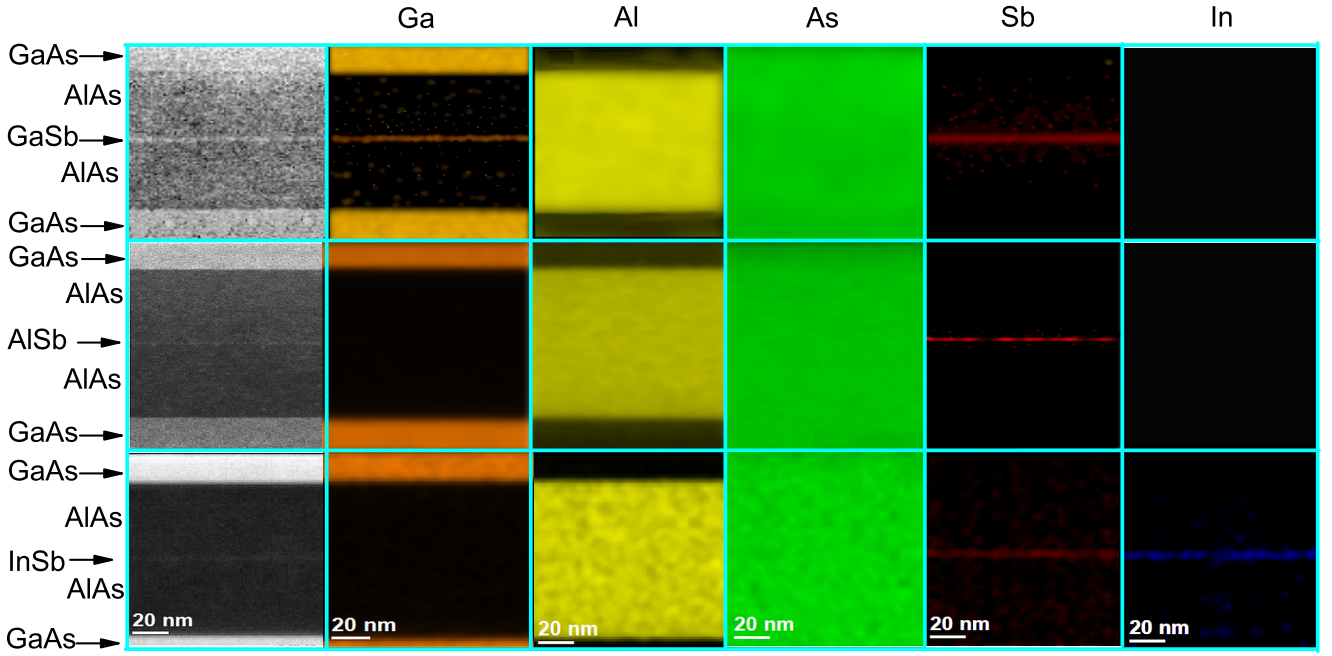


FIG. 1. TEM and chemical mapping in cross-section STEM images, obtained by the EDAX technique. From top to bottom: (Ga,Al)(Sb,As)/AlAs, Al(Sb,As)/AlAs, and (In,Al)(Sb,As)/AlAs QW heterostructures. The distribution of elements is depicted by colors: Ga orange, Al yellow, As green, Sb red, and In blue.

Here x_0 is the nominal In (Sb) composition, n is the ML index, N is the total amount of deposited indium (antimony), and R is the segregation coefficient. This model was proposed to describe segregation into ternary alloys. In our case, for structures combining GaSb/AlAs and InSb/AlAs heteropairs we expect segregation into quaternary alloys. However, it is well known that Ga does not segregate into AlAs [38,39]. Therefore, for the (Ga,Al)(Sb,As)/AlAs QWs, we have only the Sb segregation. For structures based on InSb/AlAs, segregation of both In and Sb occurs. In principle, a mutual effect of the components on their segregation is possible. However, since In and Sb are diffusing in different sublattices and their concentrations are small enough, we assume that the segregation profiles for In and Sb can be obtained independently of each other. The coefficients R for segregation of Sb and In in GaAs and AlAs were determined in different studies [30,32,33,36]. For both species, it is in the range of $0.76 < R_{\text{In}}, R_{\text{Sb}} < 0.86$, depending on the growth temperature. The microscopy data indicate a stronger segregation for antimony, which is confirmed by our recent study on the spinodal decomposition in InSb/AlAs heterostructures [40]. Therefore, we choose $R_{\text{In}} = 0.77$ and $R_{\text{Sb}} = 0.80$, which provide a longer tail for the antimony segregation. Taking into account the amount of deposited In and Sb ($N = 0.25$ ML) we calculated the profiles of the In and Sb concentrations for the $\text{In}_x\text{Al}_{1-x}\text{As}_{1-y}\text{Sb}_y$, $\text{AlAs}_{1-y}\text{Sb}_y$, and $\text{Ga}_x\text{Al}_{1-x}\text{As}_{1-y}\text{Sb}_y$ alloys, respectively, along the QW growth direction. The results of these calculations are shown in Figs. 2(a)–2(c). One can see that in all QW structures, the In and Sb fractions are extended into some diffusion layers. Contrary to that, the Ga atoms do not segregate into AlAs and accumulate at the heterojunction within a layer with a thickness of 2 ML, as shown for GaAs QWs in an (Al,Ga)As matrix [38,39,41].

B. Photoluminescence

Time-integrated PL spectra of the studied structures, measured at a temperature of 5 K with a laser pulse repetition rate of 100 kHz and excitation density of 100 mW/cm^2 , are shown in Fig. 3. The spectra show broad emission bands with maxima (full widths at half maximum) of $E_{\text{max}} = 2.040 \text{ eV}$ (190 meV) and 1.950 eV (180 meV) for the (In,Al)(Sb,As)/AlAs and Al(Sb,As)/AlAs QWs, respectively. Additionally, Fig. 3 shows the spectrum of (Ga,Al)(Sb,As)/AlAs QWs with the same nominal thickness taken from Ref. [25] for comparison, with $E_{\text{max}} = 1.850 \text{ eV}$ (170 meV). The large linewidths of the PL spectra of the studied QWs result from inhomogeneous broadening of the electron and hole energy levels due to fluctuations of the QW width and composition.

We demonstrated recently that QWs and quantum dots formed in the GaSb/AlAs and InSb/AlAs heterosystems can have both type-I or type-II band alignment, depending on the composition [10,19,40,42,43]. For AlSb/AlAs QWs with a nominal thickness of more than 1 ML, the type-II band alignment is inherent [10–12].

A method for identifying the type of band alignment in QWs with heterointerface fluctuations was proposed recently in Ref. [31]. It was shown that in such structures the PL maximum, E_{max} , measured as a function of the excitation power density, P_{ex} , is described by the following expression:

$$E_{\text{max}}(P_{\text{ex}}) - E_{\text{max}}(P_0) = (U_e + U_h)\ln(P_{\text{ex}}/P_0) + b(P_{\text{ex}}/P_0)^{1/3}. \quad (2)$$

Here U_e and U_h are the parameters of the Urbach energy tails for electrons and holes, respectively, P_0 is the minimum value of the used excitation power density, and b is a

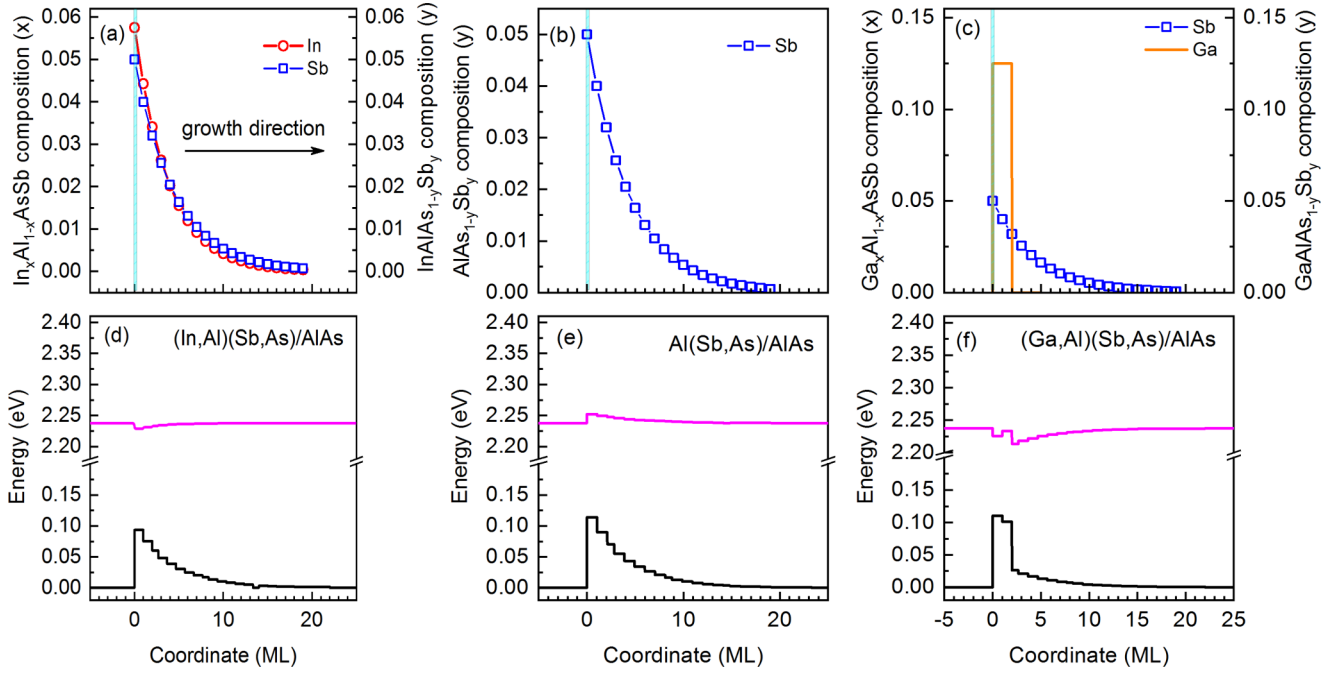


FIG. 2. Segregation profiles in interdiffused QWs with a nominal amount $N = 0.25$ ML of deposited material (shown by cyan) along the QW growth axis, calculated by using Eqs. (1) with segregation coefficients in AlAs for indium $R_{\text{In}} = 0.77$ and antimony $R_{\text{Sb}} = 0.80$, and taking into account that gallium atoms do not segregate into AlAs, for (a) In and Sb in $(\text{In,Al})(\text{Sb,As})/\text{AlAs}$, (b) Sb in $\text{Al}(\text{Sb,As})/\text{AlAs}$, and (c) Ga and Sb in $(\text{Ga,Al})(\text{Sb,As})/\text{AlAs}$ QW heterostructures. Band diagrams of the interdiffused QWs calculated for these segregation profiles in the envelope function approximation within the eight-band $\mathbf{k} \cdot \mathbf{p}$ model for electrons and holes, taking into account elastic strain in the heterostructures, using the nextnano++ simulation suite, for (d) $(\text{In,Al})(\text{Sb,As})/\text{AlAs}$, (f) $\text{Al}(\text{Sb,As})/\text{AlAs}$, and (e) $(\text{Ga,Al})(\text{Sb,As})/\text{AlAs}$. X_{xy} are the conduction band minima (magenta); the valence band has heavy hole character (black).

variable parameter. The logarithmic term describes the effect of electronic-state filling in the QWs for both type-I and type-II band alignments. The second term takes into account the

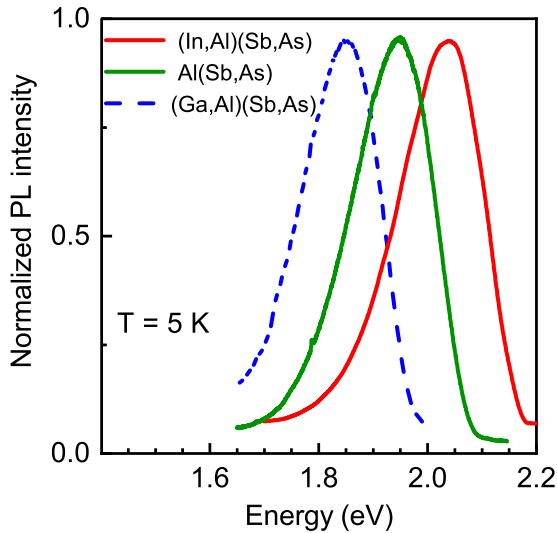


FIG. 3. Normalized time-integrated photoluminescence spectra of the $(\text{In,Al})(\text{Sb,As})/\text{AlAs}$ (red) and $\text{Al}(\text{Sb,As})/\text{AlAs}$ (green) QWs. Additionally, for comparison, we show the spectrum of the $(\text{Ga,Al})(\text{Sb,As})/\text{AlAs}$ QW (sample S1) (dashed blue) studied in Ref. [25]. The pulse repetition rate of the excitation laser is 100 kHz. $T = 5$ K.

band bending, which appears with increasing charge carrier concentration in QWs with type-II band alignment due to the spatial separation of the carriers between QW and matrix, but it is absent in QWs with type-I band alignment where $b \equiv 0$.

To determine the type of band alignment for the studied QWs, we measured the PL line energy as a function of excitation power density in the range of linear increase of the steady-state PL intensity [31]. The dependence of the PL line shift on the excitation power density [$E_{\text{max}}(P_{\text{ex}}) - E_{\text{max}}(P_0)$ for $P_0 = 10^{-3}$ W/cm²] is given in Figs. 4(a) and 4(b) for the $(\text{In,Al})(\text{Sb,As})/\text{AlAs}$ and $\text{Al}(\text{Sb,As})/\text{AlAs}$ QWs, respectively. The PL shift is well described by only the logarithmic term in Eq. (2) in the case of $(\text{In,Al})(\text{Sb,As})/\text{AlAs}$ QWs ($U_e + U_h = 1.5 \pm 0.1$ meV), while both the logarithmic ($U_e + U_h = 2.5 \pm 0.1$ meV) and $b = 0.35 \pm 0.01$ meV terms are needed for the $\text{Al}(\text{Sb,As})/\text{AlAs}$ QWs. Therefore, we can conclude that the $(\text{In,Al})(\text{Sb,As})/\text{AlAs}$ and $\text{Al}(\text{Sb,As})/\text{AlAs}$ QWs have a band alignment of type I and type II, respectively. The band diagrams of the QWs are shown schematically in the insets of Fig. 4. The characteristic (Urbach) energy tails in the densities of electron and hole states, 2.5 meV and 1.5 meV, are smaller than the value of 9.9 meV observed for $(\text{Ga,Al})(\text{Sb,As})/\text{AlAs}$ QWs in our recent study [25]. However, it is worth noting that in all cases the Urbach energy tails are several orders of magnitude smaller than the PL bandwidth. The smallness of the Urbach tail in comparison with the PL bandwidth has been explained recently [31]. The fluctuations are caused by the spatially inhomogeneous antimony segregation when overgrowing a thin InSb, AlSb, or GaSb layer with aluminum

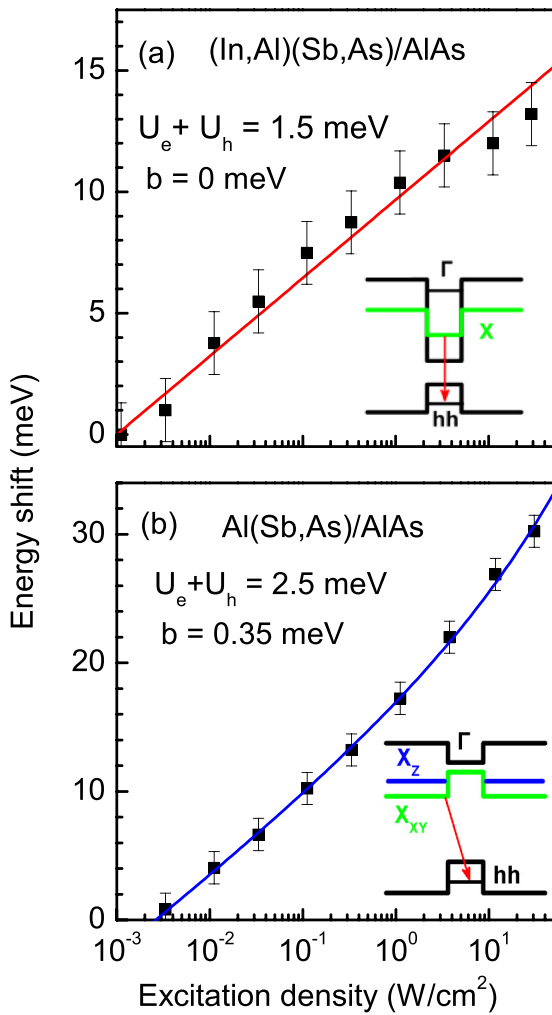


FIG. 4. Energy shift of the PL band maximum in the studied structures as function of excitation density. $T = 1.8$ K. Solid lines give the dependence according to $E_{\max}(P_{\text{ex}}) - E_{\max}(P_0) = (U_e + U_h) \ln(P_{\text{ex}}/P_0) + b(P_{\text{ex}}/P_0)^{1/3}$ meV with $P_0 = 10^{-3}$ W/cm^2 : (a) (In,Al)(Sb,As)/AlAs, (b) Al(Sb,As)/AlAs. Insets show schematically the QW band structures. The Γ and X valleys of the conduction band are presented by black and green (and blue) colors, respectively. The red arrows mark the optical transitions.

arsenide. Thus, the QWs are formed by relatively thick layers of alloy with strong spatial fluctuations of the composition both in the QW plane and along the growth direction. The energy spectrum of such QWs is given by a continuous set of fluctuations of varying size. However, for the sake of simplicity, we can divide the fluctuations into two types with different lateral sizes: (i) short-range fluctuations with lateral sizes comparable with the de Broglie wavelength of charge carriers and (ii) long-range fluctuations with lateral sizes significantly exceeding the de Broglie wavelength, resulting in the band gap (E_g) dispersion. The segments with the short-range fluctuations are responsible for the Urbach energy tails, whereas the long-range fluctuations lead to the inhomogeneous PL broadening, resulting from superposition of the spectra of all segments (see Fig. 5).

The long-range spatial fluctuations of the composition in Al-, Ga-, and In-antimony-based thin QWs are much stronger

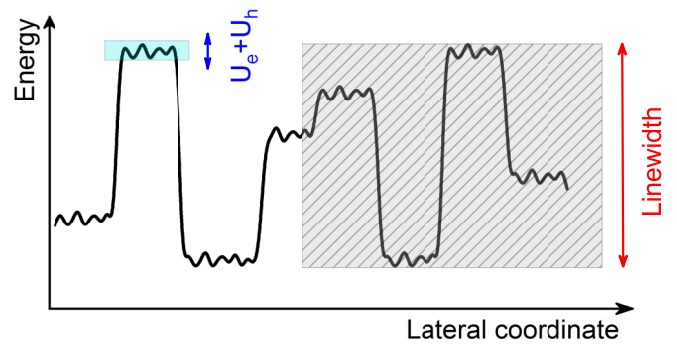


FIG. 5. Schematic illustration highlighting the effect of material composition and composition fluctuations on the QW energy spectrum. Two types of fluctuations, short-range and long-range, are responsible for the Urbach tails and linewidths, respectively, as shown in Ref. [31].

than those in Ga- and (In,Al)-arsenic-based QWs studied in recent manuscripts [21,24]. Increasing the fluctuation range leads to a stronger localization of charge carriers in the QWs that should clearly manifest in the temperature dependence of the QWs PL intensity. Figure 6 shows the PL intensity as a function of temperature measured in (In,Al)(Sb,As)/AlAs and Al(Sb,As)/AlAs QWs, as well as for (In,Al)As/AlAs [24] and GaAs/AlAs QWs [21] studied previously. One can see that the PL intensity monotonically decreases for increasing temperature in all QWs. This decrease is related to nonradiative centers at the heterointerfaces, which capture excitons more efficiently at elevated temperatures as the exciton diffusion length increases with increasing temperature due to delocalization [44–46]. However, in (In,Al)As/AlAs and GaAs/AlAs QWs, the PL intensity is decreased by about one order of magnitude for increasing temperature from 2 K up to 15 K, while in Al(Sb,As)/AlAs and (In,Al)(Sb,As)/AlAs

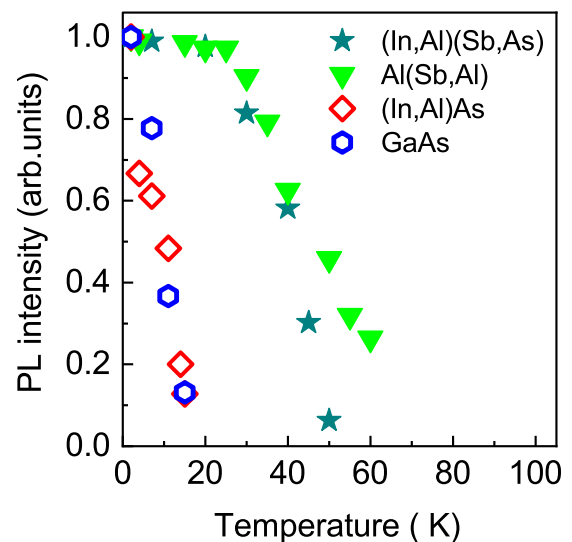


FIG. 6. Normalized PL intensity as function of temperature measured for (In,Al)(Sb,As)/AlAs, Al(Sb,As)/AlAs, (In,Al)As/AlAs [24], and GaAs/AlAs [21] thin indirect band gap QWs.

QWs the PL intensity barely changes up to 20 K and begins to decrease only for higher temperatures.

Let us have a closer look into the energy-level spectrum of the antimony-based thin QWs by computing the single-particle states in the envelope function approximation within the eight-band $\mathbf{k} \cdot \mathbf{p}$ model for electrons and holes, using the nextnano++ simulation suite. The parameters of the alloys were calculated in the quadratic approximation using the parameters of the InSb, InAs, AlSb, and AlAs binary compounds [47]. The distribution of elastic strain in the heterostructure was calculated in the solid state approximation [48] by minimizing the elastic energy. The results of the calculations are shown in Figs. 2(d)–2(f). One can see that the band alignment is of type I for (In,Al)(Sb,As)/AlAs QWs and of type II for Al(Sb,As)/AlAs QWs, which is in good accordance with the experimental observations presented here, as well as of type I for (Ga,Al)(Sb,As)/AlAs QWs as observed in Ref. [25].

C. Effect of magnetic field on photoluminescence

We found recently that a longitudinal magnetic field strongly affects the (i) PL intensity and (ii) exciton lifetime in thin indirect band gap QWs with either type-I or type-II band alignment. This effect was observed in GaAs/AlAs [21,22], (In,Al)As/AlAs [24], and (Ga,Al)(Sb,As)/AlAs [25] QWs.

Despite the fact that the studied antimony-based thin (In,Al)(Sb,As)/AlAs and Al(Sb,As)/AlAs QWs have a similar band structure, the behavior of their PL in magnetic field, as we will show in the next subsections, differs significantly from that in the previously studied thin indirect band gap QWs.

1. PL intensity in magnetic field

Time-integrated PL spectra measured in zero magnetic field and $B = 8$ T applied parallel to the growth axis (Faraday geometry) for the (In,Al)(Sb,As)/AlAs and Al(Sb,As)/AlAs QWs, are shown in Figs. 7(a) and 7(b), respectively. Surprisingly, the magnetic field does not change the PL intensity for both QWs.

The dynamics of the unpolarized PL intensity measured at the PL maximum of the (In,Al)(Sb,As)/AlAs and Al(Sb,As)/AlAs QWs are shown in Figs. 8(a) and 8(b), respectively. In both cases, the recombination dynamics show two distinct stages: (i) a fast nonexponential decay during the initial time after the excitation pulse, which is followed by (ii) an exponential decay with times of $\tau_r^{\text{InSb}} = 0.35$ ms and $\tau_r^{\text{AlSb}} = 0.38$ ms for (In,Al)(Sb,As)/AlAs and Al(Sb,As)/AlAs, respectively.

The initial short-term nonexponential dynamics arise from exciton hopping to the nearest lower energy localization site with momentum scattering of the indirect exciton. This was observed in many indirect band gap QW structures with disorder induced by fluctuations of the QW width and composition. However, since most of the PL intensity in the time-integrated spectra is collected during the times corresponding to the long-term decay, we focus in our analysis on this dynamical range.

In a longitudinal magnetic field of 8 T, the decay time of the long-term component in both structures remains unexpectedly

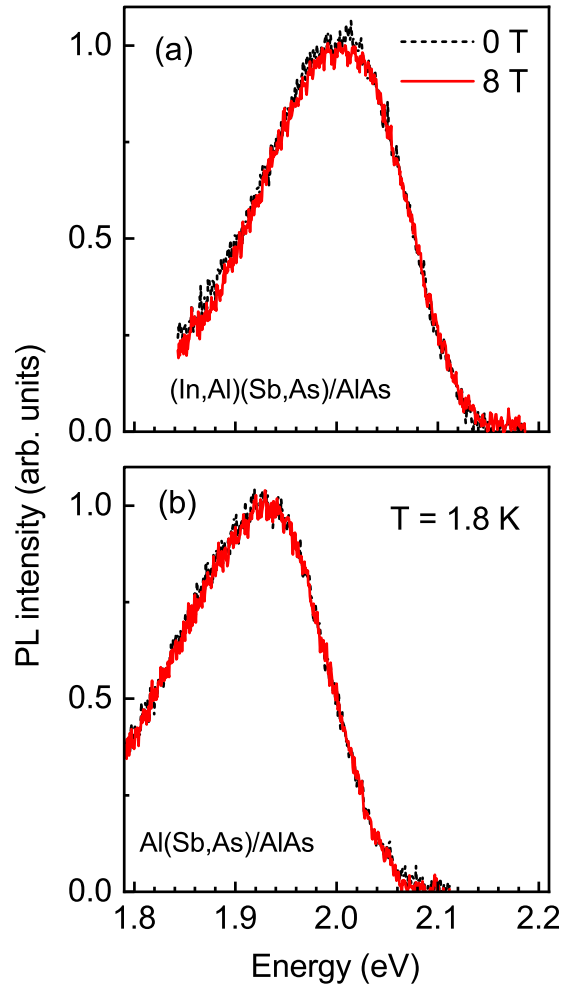


FIG. 7. Low-temperature (1.8 K) time-integrated PL spectra of the ultrathin QWs measured at magnetic fields 0 T (dashed black line) and 8 T (solid red line) in the Faraday geometry ($\mathbf{B} \parallel z$): (a) (In,Al)(Sb,As)/AlAs, (b) Al(Sb,As)/AlAs.

the same as in zero field as shown in Fig. 8. This is in contrast to other studies where it strongly slows down in other thin QWs with indirect band gap subject to a similar magnetic field (up to 25 times from 0.36 to 8.5 ms in GaAs/AlAs QWs) [21].

2. Magnetic field induced circular polarization

Application of the magnetic field in the Faraday geometry results in polarization of the emission as shown for $B = 4$ T in Figs. 9(a) and 9(b) for (In,Al)(Sb,As)/AlAs and Al(Sb,As)/AlAs QWs, respectively. One can see that P_c is positive (i.e., it is dominated by the σ^+ polarized PL component) in contrast to ML-thick GaAs/AlAs, (In,Al)As/AlAs, and (Ga,Al)(Sb,As)/AlAs QWs which show negative polarization in magnetic field [22,24,25]. The value of P_c at the PL maximum for $B = 4$ T equals 0.27 for (In,Al)(Sb,As)/AlAs QWs and 0.11 for Al(Sb,As)/AlAs QWs.

The magnetic field dependencies of P_c measured at the PL maximum in Faraday geometry, $\theta = 0^\circ$, and for tilted from the growth axis magnetic fields $\theta \in [0^\circ, 45^\circ]$ are shown in Fig. 10. The P_c for both QWs increases and reaches saturation at high magnetic fields for all θ . The polarization degree in

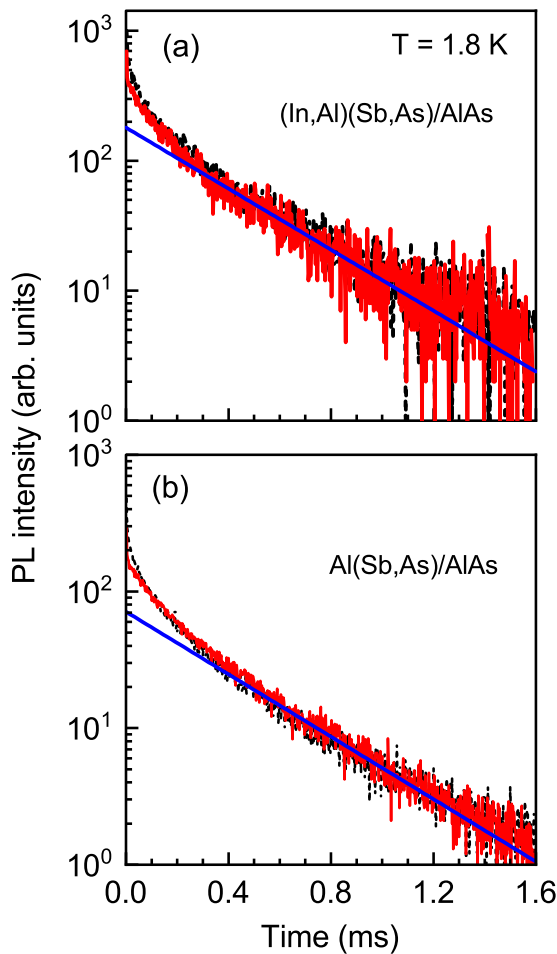


FIG. 8. Recombination dynamics measured at the PL maximum in longitudinal magnetic fields of $B = 0$ (dashed black line) and 8 T (solid red line). (a) (In,Al)(Sb,As)/AlAs QW dynamics recorded at 2.00 eV. The solid line is a monoexponential fit with $\tau_r^{\text{InSb}} = 0.35 \pm 0.02$ ms (b) Al(Sb,As)/AlAs QW dynamics recorded at 1.93 eV. The solid line is a monoexponential fit with $\tau_r^{\text{AlSb}} = 0.38 \pm 0.02$ ms. The laser pulse repetition rate is 400 Hz. The laser pulse ends at 10 ns. $T = 1.8$ K.

saturation decreases with the θ increase from 0.30 (0.12) in the Faraday geometry down to 0.22 (0.085) at $\theta = 45^\circ$ for the (In,Al)(Sb,As)/AlAs (Al(Sb,As)/AlAs) QWs. The $P_c(B)$ dependencies on θ are qualitatively different from those in the previously studied thin indirect band gap QWs. In these QWs, P_c behaves nonmonotonically in Faraday geometry. It increases at low magnetic fields before it reaches a maximum absolute value, and then decreases in strong fields (as shown, for example, in Fig. 2 of Ref. [22]). In tilted geometries, these QWs also demonstrate an increase rather than a decrease of the polarization degree in high magnetic fields (see Fig. 5 in Ref. [22]).

For a fixed longitudinal magnetic field $B = 7$ T, the $P_c(T)$ in the (In,Al)(Sb,As)/AlAs (Al(Sb,As)/AlAs) QWs demonstrates a monotonic decrease from 0.3 (0.12) at 1.6 K down to about 0.01 (0.01) at 15 K, as shown in Figs. 11(a) and 11(b). This temperature dependence is also different from other indirect band-gap QWs, which demonstrate a nonmonotonic

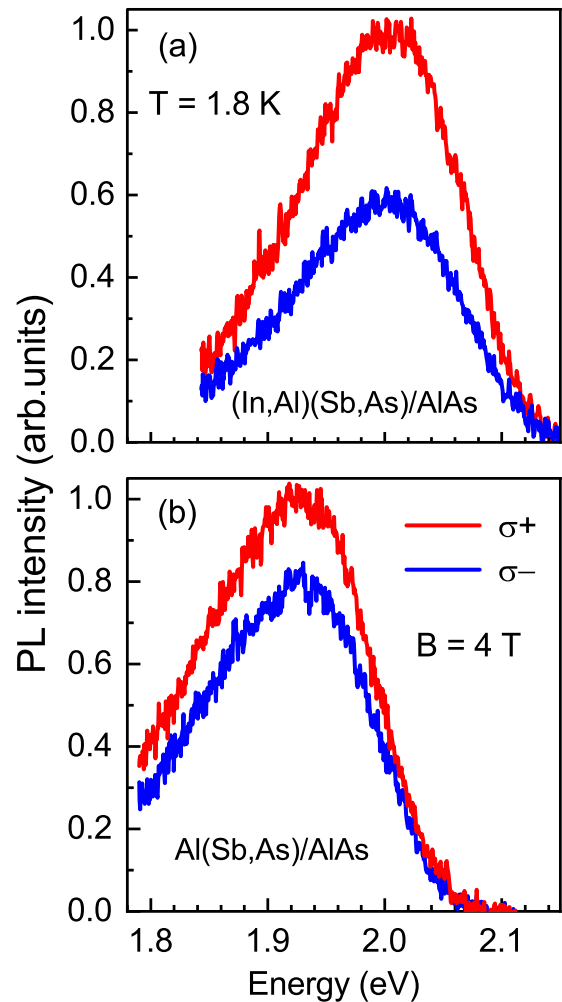


FIG. 9. Time-integrated PL spectra of the ultrathin QWs measured in Faraday geometry ($\mathbf{B} \parallel z$) at a magnetic field of 4 T in σ^+ and σ^- polarization for $T = 1.8$ K. The pulse repetition rate is 2 kHz and the emission is integrated over the temporal range of 0 – 0.5 ms: (a) (In,Al)(Sb,As)/AlAs, (b) Al(Sb,As)/AlAs.

temperature dependence of the polarization degree. $P_c(T)$ increases with growing temperature, reaches its maximum absolute value, and then decreases at higher temperatures (see Fig. 4 in Ref. [22]).

The time evolution of P_c after pulsed excitation measured at $B = 8$ T is depicted in Fig. 12. In both QWs, the polarization dynamics are unusually nonmonotonic. During the initial rise phase, which spans tens of microseconds, P_c reaches 0.40 (0.14) for the (In,Al)(Sb,As)/AlAs (Al(Sb,As)/AlAs) QWs and then tends to zero for time delays up to 1 ms.

In conclusion of this section, we summarize the most important experimental findings:

- (i) Material intermixing occurs, and the QWs consist of a quaternary $\text{In}_x\text{Al}_{1-x}\text{Sb}_y\text{As}_{1-y}$ or a ternary $\text{AlSb}_y\text{As}_{1-y}$ alloy.
- (ii) (In,Al)(Sb,As)/AlAs and Al(Sb,As)/AlAs QWs have a band alignment of type I and type II, respectively.
- (iii) Strong long-range spatial fluctuations of the composition both in the QW plane and along the growth direction result in a strong inhomogeneous broadening of the PL spectra from the (In,Al)(Sb,As)/AlAs and Al(Sb,As)/AlAs QWs.

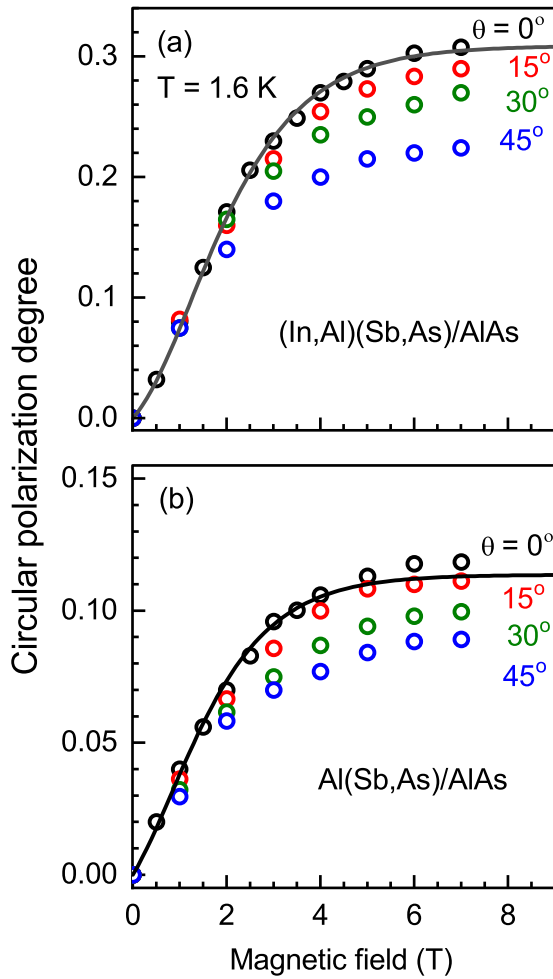


FIG. 10. Magnetic field dependence of the polarization degree measured at the maximum of the time-integrated PL of $\theta = 0^\circ$, 15° , 30° , and 45° . (a) (In,Al)(Sb,As)/AlAs QWs, (b) Al(Sb,As)/AlAs QWs. The solid lines show the results of model calculations for $\theta = 0^\circ$ using the parameters given in text.

(iv) Intensity and dynamics of the exciton radiative recombination in both (In,Al)(Sb,As)/AlAs and Al(Sb,As)/AlAs QWs do not depend on the magnetic field strength in any geometry. That is in contrast to the previously observed strong dependence of these PL parameters on the magnetic field strength in Faraday and tilted-field geometries for similar indirect band gap QWs, such as GaAs/AlAs [21,22], (In,Al)As/AlAs [24], and (Ga,Al)(Sb,As)/AlAs [25].

(v) Circular polarization P_c induced by the external magnetic field in both QWs is positive (dominated by the σ^+ polarized PL component), in contrast to previously observed negative P_c in other indirect band gap QWs [21,22,24,25].

(vi) In both QWs, $P_c(B)$ demonstrates a monotonic increase with saturation in strong fields for all angles between the growth axis and the external magnetic field. An increase of the tilt angle θ from 0° to 45° as well as temperature increase lead to a monotonic decrease of P_c for fixed B . This is opposite to results on similar indirect band-gap QWs where P_c demonstrates a nonmonotonic dependence for varying θ or temperature [21,22,24,25].

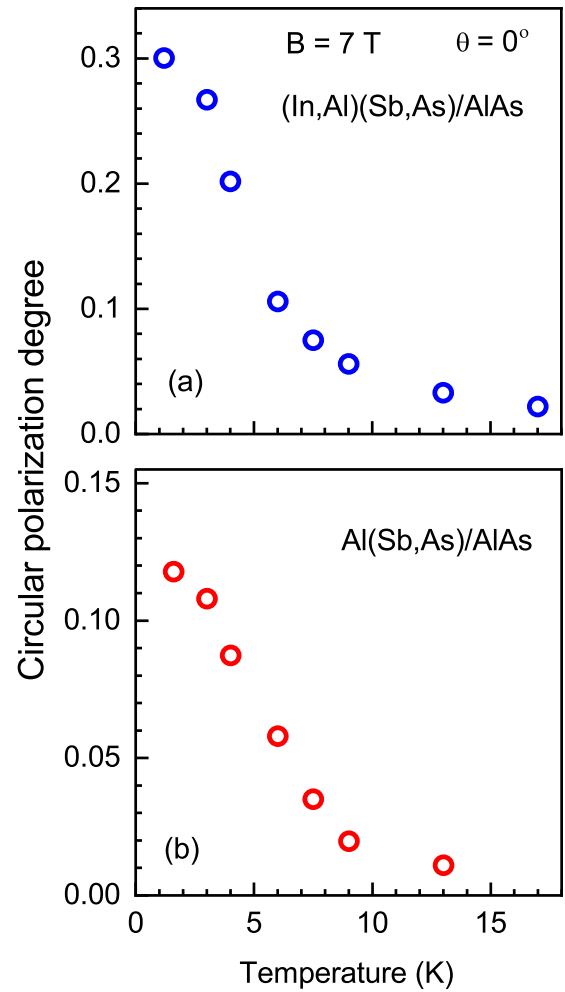


FIG. 11. Temperature dependence of the polarization degree measured at the maximum of the time-integrated PL for $\theta = 0^\circ$, $B = 7$ T. (a) (In,Al)(Sb,As)/AlAs QWs, (b) Al(Sb,As)/AlAs QWs.

(vii) Dynamics of P_c are strongly nonmonotonic in time. The P_c is increasing up to a maximum value during several tens of microseconds and then decreases to zero.

IV. DISCUSSION

We have demonstrated recently that the recombination and spin dynamics of photogenerated charge carriers in many systems containing thin indirect band gap QWs are described by a theoretical model which accounts for the fine structure spectrum of the neutral exciton [21,22]. This exciton fine structure consists of four states, according to the combinations of the angular momenta of electron and hole. The two exciton states characterized by the angular momentum projections ± 1 onto the growth z axis are bright and the two states with the projections ± 2 are nominally dark [21,22]. The bright excitons can emit light also via phonon-assisted processes. For the dark excitons, radiative recombination is forbidden by the spin-selection rules. Their lifetime is limited by nonradiative recombination, which is very inefficient in this type of QWs [21,22]. Thus, the dark exciton states have a relatively long lifetime and can act as a reservoir of excitons.

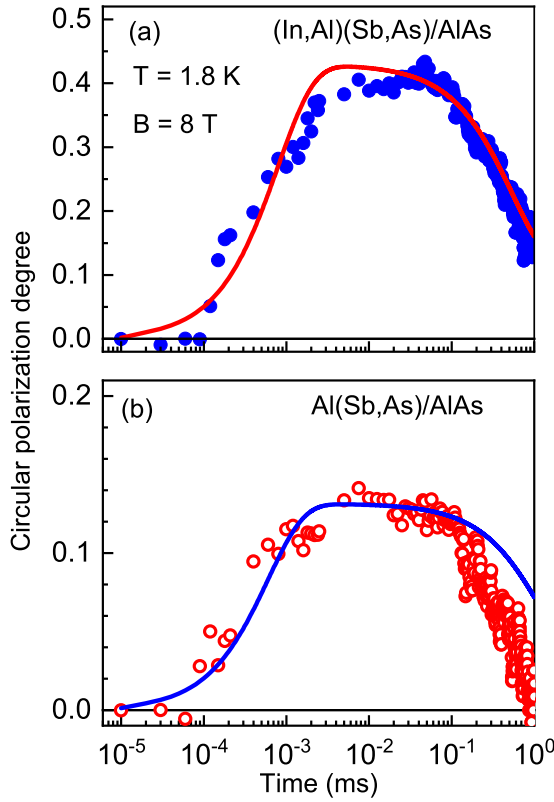


FIG. 12. Dynamics of the circular polarization degree at the maximum of the time-integrated PL line measured at $T = 1.8$ K for $B = 8$ T in the Faraday geometry: (a) (In,Al)(Sb,As)/AlAs QWs and (b) Al(Sb,As)/AlAs QWs. The solid lines show the model calculation results with the parameters given in the text.

In a magnetic field, the excitons undergo the Zeeman splitting and the dynamics of PL intensity and polarization degree are determined by the distribution of the exciton population over the bright and dark states. According to the theoretical model, the sign of P_c is determined by the signs and absolute values of the electron and hole g factors, and the ratio between the electron (τ_{se}) and heavy hole (τ_{sh}) spin-relaxation times.

Let us have a closer look at the electron and hole g factors in thin indirect band-gap QWs of both type-I and type-II band alignment, embedded in a AlAs matrix. The electron is in the X valley and its g -factor (g_e) is equal to $+2$, since due to the large band gap at the X point, the spin-orbit contribution to g_e is vanishingly small. This was demonstrated experimentally in recent studies [49–51]. The wave functions of the heavy holes in the thin QWs are predominantly localized in the AlAs matrix, therefore, the heavy hole g factor (g_{hh}) is mainly determined by the AlAs band properties. For all previously studied QWs, g_{hh} is positive and the relation $g_{hh} > g_e$ is fulfilled [21,22,24,25].

The diagram of the Zeeman splitting of the exciton for these g factors is shown schematically in Fig. 13. For $g_{hh} > g_e$, the bright exciton g factor is positive and P_c in low magnetic fields is negative. It is dominated by the lower in energy, σ^- polarized PL component as one can see in Fig. 13 for any relation between τ_{se} and τ_{sh} [22]. Additionally, in high magnetic fields the excitons mostly populate the dark state, which is

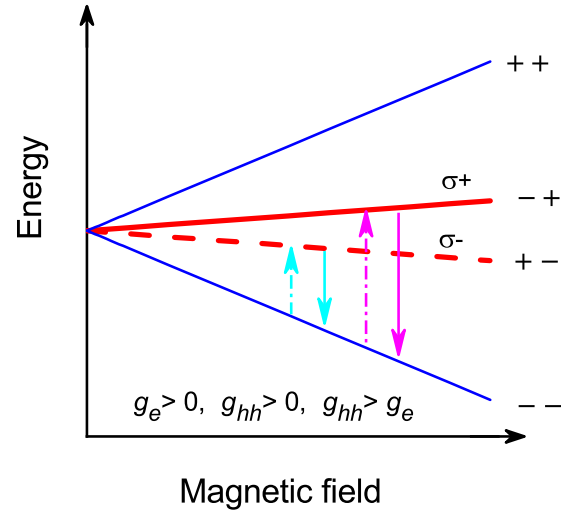


FIG. 13. Scheme of the exciton spin structure in magnetic field, applied in the Faraday geometry, $\mathbf{B} \parallel z$. The case of positive g_e and g_{hh} with $g_{hh} > g_e$ is shown. The labels $++$, $--$, $-+$, and $+ -$ correspond, respectively, to the exciton states with spin projection $+2$, -2 , $+1$, and -1 . The blue lines show the optically dark (spin-forbidden) states. The red lines show the bright (spin-allowed) states that result in σ^+ (solid line) or σ^- (dashed line) polarized emission. The arrows indicate electron (hole) spin-flip processes increasing (dash-dotted) and decreasing (solid) the carrier energy, respectively.

the lowest in energy, which should result in slowing down the recombination and reducing the PL intensity with increasing field, as observed in our recent studies [21,22,24,25]. However, one can clearly see that the experimental data obtained here contradict to the previous observations and cannot be explained within the exciton model.

The main difference in the energy-level spectrum of the antimony-based thin indirect band gap QWs studied here in comparison to arsenic-based GaAs/AlAs and (In,Al)As/AlAs QWs is the strong energy dispersion of the electron and hole states due to long-range spatial fluctuations of the QW width and composition. We assume that under conditions of such a strong dispersion of the energy levels, spatial separation of the photogenerated charge carriers in the QW plane is possible, as shown in Fig. 14. This spatial separation will lead to formation of positively and negatively charged trions, so the experimentally observed dynamics of the PL intensity and polarization will be determined by the sum of the contributions from these oppositely charged excitons. We show below that such a trion-based model of the PL accounts for all key experimental observations.

A. Theory

In this section, we present a kinetic theory of the PL polarization taking into account trion states. The main assumption in our model is that photogenerated charge carriers separate in space and, in the course of energy relaxation, trions are formed. The negative trion, T^- , consists of two electrons in the spin-singlet state and a hole with unpaired spin. The positive trion, T^+ , consists of the two holes in the spin-singlet state and an electron. We assume that the trions right after

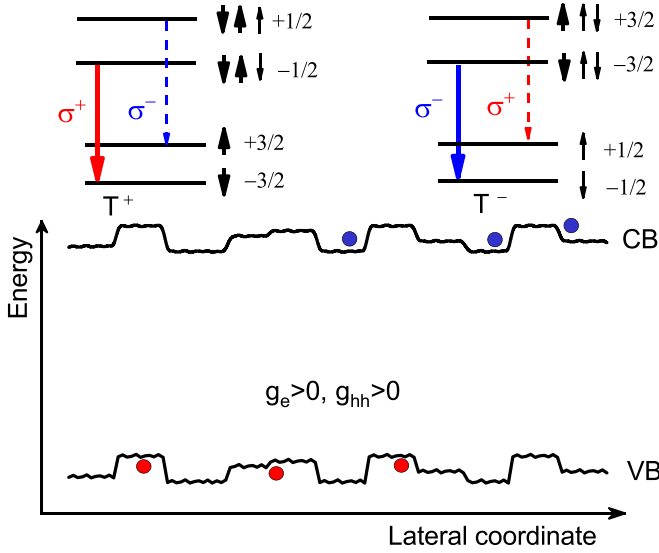


FIG. 14. Schematic illustration of the spatial separation of photogenerated charge carriers in a QW with strong energy dispersion of the electron (blue circles) and hole (red circles) states. Insets show the fine structure of positively and negatively charged trion spin states, undergoing the Zeeman splitting. The thick (thin) arrows correspond to dominating (suppressed) optical transitions in emission.

formation are unpolarized, i.e., the relaxation of the charge carriers in energy and the formation of trions occur faster than the spin relaxation of electrons and holes. Note that in the opposite case where the trions form from unpolarized excitons and polarized carriers, the PL emission polarization monitors the polarization of the resident carriers, as considered in Ref. [52]. The trions can be characterized by the spin of the unpaired charge carrier: the hole for the T^- trion and the electron for the T^+ trion. We introduce $f_{\pm 3/2}$, the number of negative trions with the hole-spin component $\pm 3/2$ on the growth axis, and $f_{\pm 1/2}$, the number of positive trions with the electron-spin component $\pm 1/2$. Neglecting conversion between T^+ and T^- trions, we obtain two independent sets of kinetic equations for the trion dynamics:

$$\frac{df_{+3/2}}{dt} + \frac{f_{+3/2}}{\tau_r} + W_{-3/2,3/2}f_{+3/2} - W_{3/2,-3/2}f_{-3/2} = G_{+3/2}(t), \quad (3a)$$

$$\frac{df_{-3/2}}{dt} + \frac{f_{-3/2}}{\tau_r} - W_{-3/2,3/2}f_{+3/2} + W_{3/2,-3/2}f_{-3/2} = G_{-3/2}(t), \quad (3b)$$

and

$$\frac{df_{+1/2}}{dt} + \frac{f_{+1/2}}{\tau_r} + W_{-1/2,1/2}f_{+1/2} - W_{1/2,-1/2}f_{-1/2} = G_{+1/2}(t), \quad (3c)$$

$$\frac{df_{-1/2}}{dt} + \frac{f_{-1/2}}{\tau_r} - W_{-1/2,1/2}f_{+1/2} + W_{1/2,-1/2}f_{-1/2} = G_{-1/2}(t). \quad (3d)$$

Here τ_r is the trion recombination rate (accounting for both the radiative and nonradiative channels) and $W_{j,-j}$ and $W_{s,-s}$ are

the hole-in-the-trion ($j = \pm 3/2$) and the electron-in-the-trion ($s = \pm 1/2$) spin-flip rates, $G_j(t)$ and $G_s(t)$ are the generation rates.

The spin-flip rates $W_{j,-j}$ and $W_{s,-s}$ depend on the magnetic field. The main effect here is the field-induced Zeeman splitting, which suppresses the transitions with increasing the electron or hole energy. Correspondingly, the spin-flip rates can be recast as [21,23]

$$W_{1/2,-1/2} = \frac{1}{2\tau_{se}} \exp\left(-\frac{g_e\mu_B B_z}{k_B T}\right), \quad (4a)$$

$$W_{3/2,-3/2} = \frac{1}{2\tau_{sh}} \exp\left(-\frac{g_{hh}\mu_B B_z}{k_B T}\right), \quad (4b)$$

$$W_{-1/2,1/2} = \frac{1}{2\tau_{se}}, \quad (4c)$$

$$W_{-3/2,3/2} = \frac{1}{2\tau_{sh}}. \quad (4d)$$

Here $k_B T$ is the temperature measured in energy units, g_e and g_{hh} are the corresponding Landé factors, and τ_{se} , τ_{sh} are the spin-flip times for the electron in the trion and hole in the trion. In Eqs. (4), we assumed that $g_e\mu_B B_z$, $g_{hh}\mu_B B_z > 0$, so the transitions $-1/2 \rightarrow 1/2$ and $-3/2 \rightarrow 3/2$ are suppressed by the Zeeman effect. For simplicity, we neglect the relatively weak, power-law [15] dependence of τ_{se} and τ_{sh} on the magnetic field. Note that the set of Eqs. (3) can be transformed into decoupled equations for the trion populations:

$$T_+ = f_{-1/2} + f_{+1/2}, \quad T_- = f_{-3/2} + f_{+3/2}, \quad (5)$$

in the form of $dT_{\pm}/dt + T_{\pm}/\tau_r = G_{\pm}(t)$ and equations for the carrier-in-the-trion spin polarization.

The set Eqs. (3) allows us to find the total number of trions,

$$T_{\text{tot}}(t) = \sum_{s=\pm 1/2} f_s + \sum_{j=\pm 3/2} f_j, \quad (6)$$

and the polarization degree of emission,

$$P_c(t) = \xi \frac{\sum_{j=\pm 3/2} (2j/3) f_j - \sum_{s=\pm 1/2} 2s f_s}{T_{\text{tot}}(t)}, \quad (7)$$

where we took into account the fact that the T^+ trion with the electron-spin component $\pm 1/2$ emits a σ^{\mp} photon and the T^- trion with the heavy-hole spin component $\pm 3/2$ emits a σ^{\pm} photon. In Eq. (7), we have also introduced a phenomenological depolarization factor $0 < \xi < 1$ [22] accounting for the deviation of the selection rules from the pure ones and also taking into account the loss of polarization of emitted light during its propagation in the structure.

B. Modeling the experimental data

The model has a fair number of parameters. The PL intensity and polarization are governed by the following set of parameters: the values and signs of the electron and hole g factors, the magnetic field strength, the radiative recombination times, the spin-relaxation rates describing the spin flip rates for downward transitions, i.e., from the upper to the lower Zeeman sublevel, and the temperature which determines the ratio of upward and downward transitions. Some of these parameters can be directly measured in experiment, others

TABLE I. Parameters of the studied thin (In,Al)(Sb,As)/AlAs and Al(Sb,As)/AlAs QWs evaluated from best fits to the experimental data. The parameters for similar indirect band-gap thin QWs of (Ga,Al)(Sb,As)/AlAs, taken from Ref. [25], of GaAs/AlAs [22], and (In,Al)As/AlAs [24] are given for comparison.

Parameter	(In,Al)(Sb,As)/AlAs	Al(Sb,As)/AlAs	(Ga,Al)(Sb,As)/AlAs	GaAs/AlAs	(In,Al)As/AlAs	Comment
g_e	+2.0	+2.0	+2.0	+2.0	+2.0	[49–51]
$g_{hh\parallel}$	$+3.6 \pm 0.3$	$+3.5 \pm 0.3$	+2.5	+3.5	+3.6	best fit
τ_r	$350 \pm 20 \mu\text{s}$	$380 \pm 20 \mu\text{s}$	$320 \mu\text{s}$	$340 \mu\text{s}$	$130 \mu\text{s}$	best fit
τ_{nr}	–	–	$430 \mu\text{s}$	$8500 \mu\text{s}$	$2100 \mu\text{s}$	–
τ_{sh}	$270 \pm 20 \mu\text{s}$	$600 \pm 50 \mu\text{s}$	$0.03 \mu\text{s}$	$3 \mu\text{s}$	$16 \mu\text{s}$	best fit
τ_{se}	$0.4 \pm 0.1 \mu\text{s}$	$0.3 \pm 0.1 \mu\text{s}$	$0.1 \mu\text{s}$	$33 \mu\text{s}$	$25 \mu\text{s}$	best fit
ξ	0.75 ± 0.02	0.25 ± 0.02	0.25	0.75	0.65	best fit
C_d	–	–	0.002	0.001	0.0015	–
N_{T^+}/N_{T^-}	1.35 ± 0.03	1.25 ± 0.03	–	–	–	best fit
P_c	positive	positive	negative	negative	negative	–
Band alignment	type I	type II	type I	type II	type I	–

can be evaluated from fits of the various experimental dependencies, or at least the ratio of parameters and their possible ranges of values can be found. As a result, we obtain quite stringent estimates of the parameter values.

Let us start from well-defined parameters. Due to the large band gap at the X point, the spin-orbit contribution to the electron g factor is vanishingly small [53]. As a result, the electron g factor, g_e , is isotropic and its value almost coincides with the free-electron Landé factor of +2.0 [49–51]. The recombination time of the exciton complexes can be unambiguously determined from PL dynamics measurements (Fig. 8). The solution of Eqs. (3) for pulsed excitation was used to calculate the $P_c(t)$ dynamics after Eq. (7). The analysis of the calculated results demonstrates that the rise time of the polarization degree is uniquely determined by the shortest, while the decay time of the polarization degree (Fig. 12) is given by the longest of the electron and hole spin-relaxation times and does not depend on other parameters. Thus we have just three variable parameters to describe the experimental findings: the heavy-hole longitudinal g factor g_{hh} , which is determined mainly by the AlAs band properties and has to be close to the g_{hh} value in previously studied thin QWs in a AlAs matrix [24], the depolarization factor ξ and the ratio of concentrations of the positive T^+ and negative T^- trions, Eqs. (5). However, the variation ranges of these parameters are limited. The best fits to the PL decay $\propto T_{\text{tot}}(t)$, as well as to the time-integrated and time-resolved polarization $P_c(B)$ and $P_c(t)$ at different magnetic fields are shown by the lines in Figs. 8, 10, 12. A small deviation of about 10% only in the value of depolarization factor ξ ruins already the agreement of calculation with the experimentally observed time-integrated and time-resolved polarization degree of PL. All of them are obtained with one set of parameters collected in Table I. One can see that the unusually nonmonotonic $P_c(t)$ dependence is result of the difference in τ_{sh} and τ_{se} where both of them are shorter than τ_r . In the time range $\tau_{se} < t < \tau_{sh}$, P_c is determined by the T^+ trion emission which is dominated by σ^+ polarized component due to the fast electron spin relaxation, while the T^- trion emission in this time range is still unpolarized. For $t \geq \tau_{sh}$, the heavy-hole spin relaxation polarizes the T^- trion whose emission is dominated by the σ^- polarized component. Addition of the σ^- polarized emission from the T^- trion to

the σ^+ polarized emission by the T^+ trion leads to a decreasing P_c for times $\geq \tau_{sh}$.

It is interesting to compare the parameters obtained for the thin antimony-based (In,Al)(Sb,As)/AlAs, Al(Sb,As)/AlAs QWs with those of similar thin indirect band gap QWs [22,24,25]. For all QWs under consideration, one can note some general features: (i) The same value of the electron g factor $g_e = +2$, which is determined by a negligible contribution of the spin-orbit interaction at the X point of the conduction band. (ii) Similar values of the heavy hole g factors since the hole wave function is localized predominantly in the AlAs matrix, and $g_{hh} > 0$. (iii) Similar values of the long radiative recombination times of the exciton complexes, which reflect the momentum separation of electrons and holes in structures with an indirect band gap.

On the other hand, one can divide the QWs into two groups, namely, the arsenic- and antimony-based ones. These groups differ in their atomic structures and the related features in the QW energy-level structures. The arsenic-based QWs [(In,Al)As/AlAs and GaAs/AlAs] demonstrate relatively small spatial fluctuations of the material composition. These fluctuations have lateral sizes, which mainly do not exceed de Broglie wavelength of the charge carriers. Electrons and holes captured in such QWs from the matrix form neutral excitons. Therefore, the recombination and spin dynamics in these arsenic-based QWs are determined by the redistribution of excitons between their bright and dark states. The antimony-based QWs [(In,Al)(Sb,As)/AlAs and Al(Sb,As)/AlAs] show strong spatial fluctuations with lateral sizes significantly exceeding the de Broglie wavelength. The spatial separation of photogenerated charge carriers in the QW plane provides the formation of charged excitons. The recombination and spin dynamics in these QWs are determined by the cumulative contribution of positive and negative trions.

Note that the behavior of the (Ga,Al)(Sb,As)/AlAs QWs studied in Ref. [25] does not fit into the pure neutral or pure charged exciton picture. Indeed, some samples with such QWs demonstrate features inherent to the neutral exciton dynamics (deceleration of exciton recombination in a longitudinal magnetic field and increase of polarization degree in a tilted magnetic field), while other samples show a very small (down to zero) polarization degree in a longitudinal

magnetic field that can rather be explained by the simultaneous recombination of trions of different polarity (similar to other antimony-based QWs). We believe that these heterostructures can have atomic structures (and, accordingly, energy-level spectra) that contribute to the formation of both neutral and charged excitons. The spatially inhomogeneous antimony distribution leads to antimony-depleted and enriched regions. The structure of the first region is close to the one in GaAs/AlAs QWs and that of the other one is rather close to Al(Sb,As)/AlAs QWs. The dominance of one or the other region inside (Ga,Al)(Sb,As)/AlAs QWs is determined by the growth condition.

V. MODEL PREDICTION FOR STRUCTURES WITH DIFFERENT SETS OF PARAMETERS

In this section, we use the developed model to simulate the experimental phenomena in structures with different parameters to show the variability of possible experimental situations. This can serve as a guide for the further search for systems with tailored dependencies of the degree of polarization on the magnetic field. For illustration of the model predictions, we select those dependencies that clearly demonstrate distinct features for the chosen sets of parameters: the dynamics of P_c at fixed magnetic field strength and $P_c(B)$ in longitudinal magnetic field. Hereinafter, we choose for definiteness as value of the recombination time $\tau_r = 1$ ms and of the electron g factor $g_e = +2$ in all calculations. The kinetic parameter ratios are taken as $\tau_{se}/\tau_{sh} = 0.01, 0.1, 1, 10, 100$. The ratio $\tau_{se}/\tau_{sh} = 1$ corresponds to $\tau_{se} = 0.1$ ms, $\tau_{sh} = 0.1$ ms. For values of 0.01 and 0.1, the τ_{se} is decreased to $\tau_{sh} = 0.1$ ms, while for values of 10 and 100 the τ_{sh} is decreased to $\tau_{se} = 0.1$ ms. For simplicity, we set the depolarization factor $\xi = 1$.

A. Exclusively negatively/positively charged trions

Let us start from the well-known simple case when a system contains only one type of trion. A negative (positive) trion, T^- (T^+) consists of two electrons (heavy holes) and one heavy hole (electron); after its recombination, a resident carrier is left in the QW. The fine structure of the involved states split by a magnetic field is determined by the magnitude and sign of the heavy-hole and electron g factors as shown in Fig. 15 [54,55]. One can see that the sign of the magnetic-field-induced circular polarization is uniquely determined by the g factor of the heavy hole (electron) for the negative (positive) trion. P_c is dominated by the σ^+ (σ^-) polarized PL component in the case of $g_{hh} < 0$ ($g_{hh} > 0$) for T^- and of $g_e > 0$ ($g_e < 0$) for T^+ trions.

For definiteness, we select the case $g_e > 0$ and $g_{hh} > 0$ and calculate $P_c(B)$ for different carrier spin relaxation times ($\tau_{sh} = 0.1$ ms, $\tau_{se} = 0.1, 0.01, \text{ and } 0.001$ ms) and g factors ($g_{hh} = 1, 2, \text{ and } 4$). $P_c(B)$ increases with increasing magnetic field with saturation at high field strengths (Fig. 16). The saturation level, as shown for T^+ in Fig. 16(a), is determined by the τ_{se}/τ_r ratio and increases with decreasing τ_{se} . On the other hand, the rise of the polarization degree is determined by the g -factor value, as shown in Fig. 16(b) for T^- . For high magnetic fields, in the range of saturation of $P_c(B)$, the dynamics of the polarization degree are determined only by

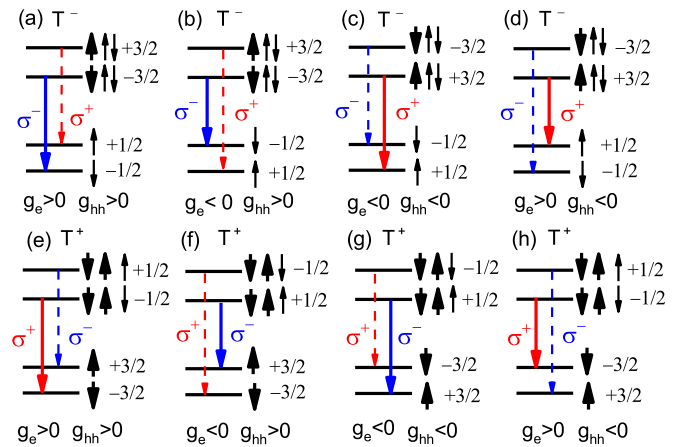


FIG. 15. Schematic illustration of energy states that undergo the Zeeman splitting of negatively (a)–(d) and positively (e)–(h) charged trions composed of electrons and heavy holes covering different combinations of g factors: (a) and (e) $g_e > 0$, $g_{hh} > 0$, (b) and (f) $g_e < 0$, $g_{hh} > 0$, (c) and (g) $g_e < 0$, $g_{hh} < 0$, (d) and (h) $g_e > 0$, $g_{hh} < 0$. The thick solid (thin dashed) arrows relate to dominating (suppressed) optical transitions in emission.

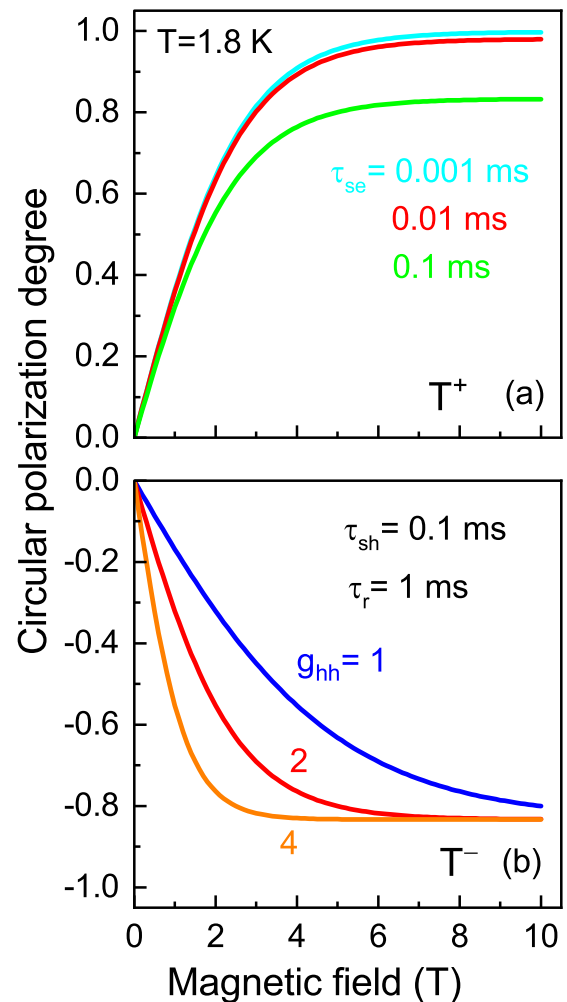


FIG. 16. Magnetic field dependence of the PL circular polarization degree calculated in case of $g_e > 0$ and $g_{hh} > 0$ for (a) T^+ with $\tau_{se} = 0.1, 0.01, \text{ and } 0.001$ ms and (b) T^- with $\tau_{sh} = 0.1$ ms, $g_{hh} = 1, 2, \text{ and } 4$. We assume in the calculations $T = 1.8$ K and $\tau_r = 1$ ms.

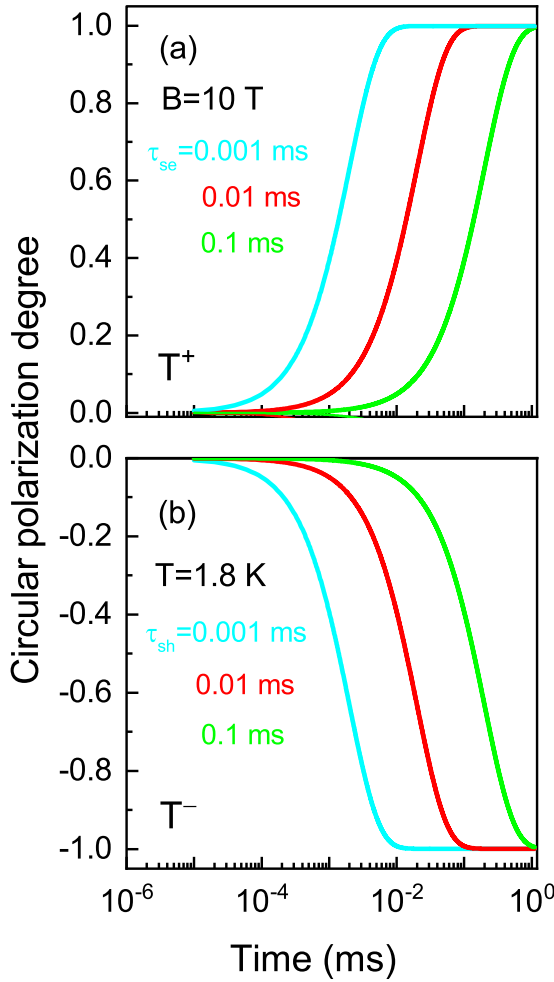


FIG. 17. Dynamics of the circular polarization degree calculated in case of $g_e > 0$ and $g_{hh} > 0$ for the PL of (a) T^+ with $\tau_{se} = 0.1, 0.01, \text{ and } 0.001$ ms and (b) T^- with $\tau_{sh} = 0.1, 0.01, \text{ and } 0.001$ ms in a magnetic field of 10 T. We assume in the calculations $T = 1.8$ K and $\tau_r = 1$ ms.

the spin relaxation times of the charge carriers, as shown in Figs. 17(a) and 17(b). Note that the results in Fig. 17(b) for T^- are the same for g_{hh} , equal to 1, 2, and 4.

B. Combinations of positively and negatively charged trions

Let us now analyze the situation of coexistence of T^+ and T^- trions that can, for example, be realized for spatial separation of electrons and holes in a system with disorder. Two different cases are possible in such systems where the P_c signs for T^+ and T^- (1) differ [for example, Figs. 15(a) and 15(e)] and (2) coincide [for example, Figs. 15(d) and 15(h)].

1. Different signs of magnetic-field-induced circular polarization for T^+ and T^-

We first consider the situation where the signs of the magnetic-field-induced polarization from the T^+ and T^- related PL are different. We also consider the case $g_e > 0$ and $g_{hh} > 0$ for definiteness. The scenarios for $g_e > g_{hh}$ and $g_e < g_{hh}$ for a set of different ratios of τ_{se}/τ_{sh} as well as ratios of concentrations of positive (N_{T^+}) and negative (N_{T^-}) trions are

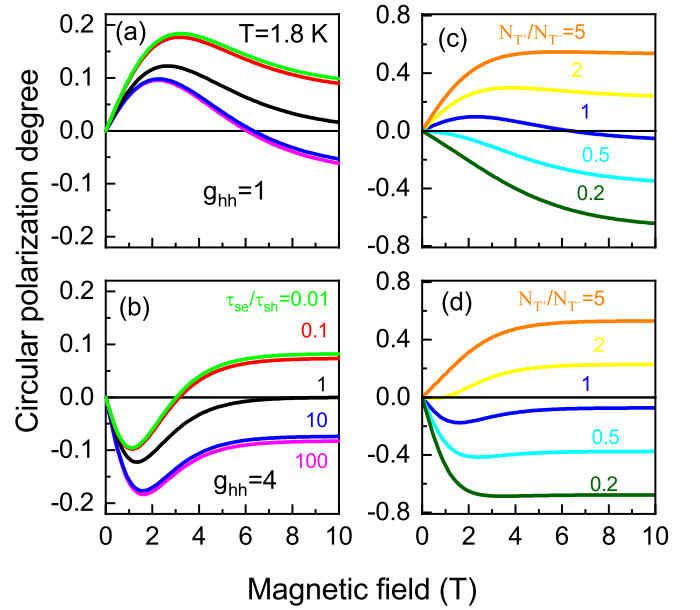


FIG. 18. Magnetic-field dependence of P_c calculated for a set of different ratios of τ_{se}/τ_{sh} and N_{T^+}/N_{T^-} at $T = 1.8$ K: (a) $g_e = 2$ and $g_{hh} = 1, N_{T^+}/N_{T^-} = 1, \tau_{se}/\tau_{sh} = 0.01, 0.1, 1, 10, 100$. (b) $g_e = 2$ and $g_{hh} = 4, N_{T^+}/N_{T^-} = 1, \tau_{se}/\tau_{sh} = 0.01, 0.1, 1, 10, 100$. (c) $g_e = 2$ and $g_{hh} = 1, \tau_{se}/\tau_{sh} = 10, N_{T^+}/N_{T^-} = 0.2, 0.5, 1, 2, 5$. (d) $g_e = 2$ and $g_{hh} = 4, \tau_{se}/\tau_{sh} = 10, N_{T^+}/N_{T^-} = 0.2, 0.5, 1, 2, 5$.

shown in Fig. 18. For the case of equal concentrations of T^+ and T^- , $P_c(B)$ is a nonmonotonic function. The absolute value $|P_c|$ increases in low magnetic fields, but decreases in high fields. The details of the $P_c(B)$ dependencies are determined by the ratios of the carrier g factors and the kinetic parameter ratio τ_{se}/τ_{sh} , as one can see in Figs. 18(a) and 18(b). On the

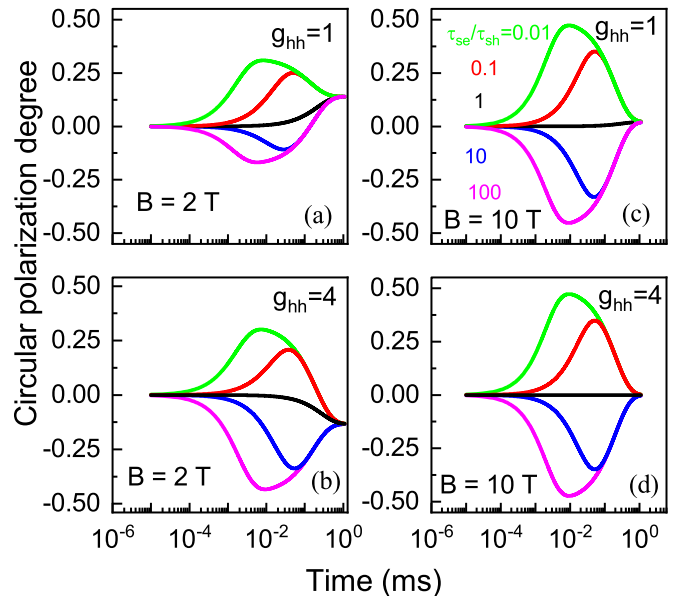


FIG. 19. Dynamics of P_c calculated for a set of different ratios of $\tau_{se}/\tau_{sh} = 0.01, 0.1, 1, 10, 100$, and $N_{T^+}/N_{T^-} = 1$ at $T = 1.8$ K: (a) $g_e = 2$ and $g_{hh} = 1, B = 2$ T. (b) $g_e = 2$ and $g_{hh} = 4, B = 2$ T. (c) $g_e = 2$ and $g_{hh} = 1, B = 10$ T. (d) $g_e = 2$ and $g_{hh} = 4, B = 10$ T.

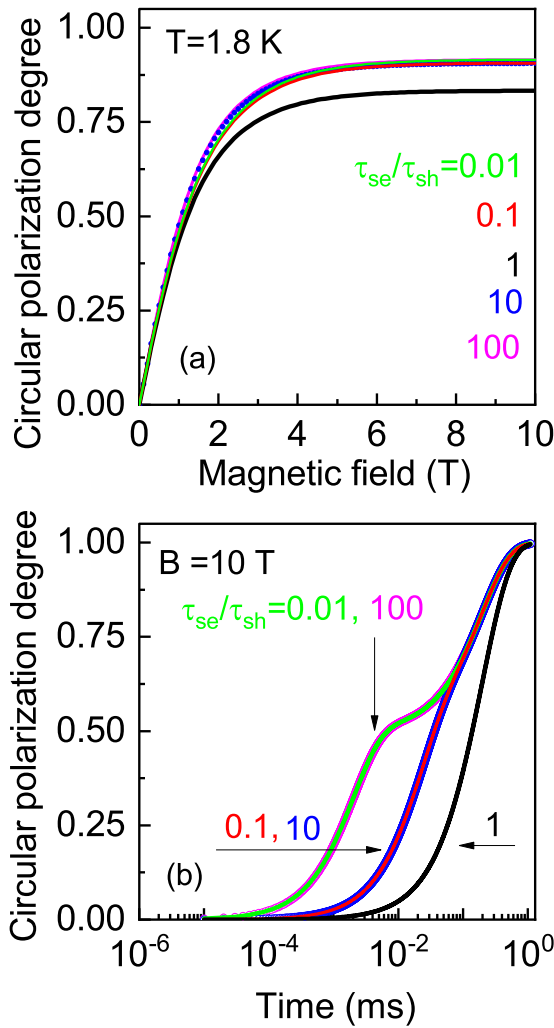


FIG. 20. Calculation of P_c for $g_e = 2$ and $g_{hh} = -4$. $T = 1.8$ K for a set of different ratios $\tau_{se}/\tau_{sh} = 0.01, 0.1, 1, 10, 100$, and $N_{T^+}/N_{T^-} = 1$: (a) magnetic field dependence, (b) dynamics at $B = 10$ T.

other hand, $P_c(B)$ tends to a monotonic growth dependence if the concentration of one trion species starts to dominate, see Figs. 18(c) and 18(d).

The dynamics of P_c in magnetic fields of $B = 2$ T and 10 T as well as $P_c(B)$ of the time-integrated PL in case of equal concentrations N_{T^+} and N_{T^-} of trions were calculated for different ratios of the carrier g factors (see Fig. 19). One can see that $P_c(t)$ behaves nonmonotonically for any magnetic field, behaving similarly for any carrier g factor values, and is determined by the kinetic parameter ratio τ_{se}/τ_{sh} .

2. Same signs of magnetic-field-induced circular polarizations for T^+ and T^-

Now we turn to the situation when the P_c signs of the T^+ and T^- trions are the same. We consider the case of $g_e > 0$

and $g_{hh} < 0$. P_c was calculated for $N_{T^+}/N_{T^-} = 1$ and different kinetic parameter ratios $\tau_{se}/\tau_{sh} = 0.01, 0.1, 1, 10, 100$ with $\tau_r = 1$ ms as a function of magnetic field [Fig. 20(a)]. The P_c dynamics calculated for the same set of parameters at $B = 10$ T are shown in Fig. 20(b). $P_c(B)$ is a monotonic function of magnetic field, converging to saturation. Its growth and saturation level are determined by the kinetic factor—the ratio of the trion lifetime to the shortest among the electron and hole spin-relaxation times. This case is not suitable for the interpretation of the experimental data. With respect to the $P_c(B)$ dynamics in high magnetic field, we can detect contributions from the two trion species only for the case when the spin relaxation times of electrons and holes are strongly different. However, even in this case it is impossible to find out which carrier (electron or hole) has a longer spin relaxation time since the $P_c(t)$ dependence is determined by the shortest among them [for example, here the ratios $\tau_{se}/\tau_{sh} = 0.01$ and 100 result in the same $P_c(t)$ curves].

VI. CONCLUSION

We have investigated experimentally and theoretically the magneto-optical properties of ultrathin indirect band gap QWs with band alignment of type I in (In,Al)(Sb,As)/AlAs and type II in Al(Sb,As)/AlAs, both with strong spatially nonuniform intermixing of the well and barrier materials. The spatial separation of electron and hole in the QW plane results in a specific situation with a coexistence of negatively and positively charged excitons in the QW. A kinetic equation model, which accounts for the population dynamics of these trions states, has been developed. Quantitative description of all experimental data is obtained with just a few variables, which can be unambiguously determined from the experimental data. We demonstrate that the magnetic field-induced circular polarization can be controlled either by thermodynamic parameters, i.e., the ratio of the exciton Zeeman splitting and the thermal energy, or by kinetic parameters, i.e., the relation between the various relaxation times in the system, depending on the magnetic field as well as on the ratio of positive and negative trion concentrations. The developed approach can be readily used for the investigation of the spin dynamics in alloy-disordered semiconductor QW structures with indirect band gap, either in real or reciprocal space, or in both of them.

ACKNOWLEDGMENTS

This work was supported by the Deutsche Forschungsgemeinschaft via Project No. 409810106. Sample growth and microscopy study, investigations of the energy-level spectrum, magneto-optical properties as well as recombination and spin dynamics of excitons were supported by a grant of the Russian Science Foundation (Grant No. 22-12-00022). The theoretical work by M.M.G. was supported by the Russian Foundation for Basic Research Grant No. 19-52-12038.

[1] C. F. Klingshirn, *Semiconductor Optics* (Springer-Verlag, Heidelberg, 2012).

[2] *Optical Generation and Control of Quantum Coherence in Semiconductor Nanostructures*, edited by G.

- Slavcheva and P. Roussignol (Springer-Verlag, Berlin, 2010).
- [3] *Spin Physics in Semiconductors*, edited by M. I. Dyakonov (Springer, Berlin, 2008).
- [4] N. Somaschi, V. Giesz, L. De Santis, J. C. Loredo, M. P. Almeida, G. Hornecker, S. L. Portalupi, T. Grange, C. Anton, J. Demory, C. Gomez, I. Sagnes, N. D. Lanzillotti-Kimura, A. Lemaitre, A. Auffeves, A. G. White, L. Lanco, and P. Senellart, Near-optimal single-photon sources in the solid state, *Nat. Photonics* **10**, 340 (2016).
- [5] M. W. Wu, J. H. Jiang, and M. Q. Weng, Spin dynamics in semiconductors, *Phys. Rep.* **493**, 61 (2010).
- [6] D. S. Smirnov, T. S. Shamirzaev, D. R. Yakovlev, and M. Bayer, Dynamic Polarization of Electron Spins Interacting with Nuclei in Semiconductor Nanostructures, *Phys. Rev. Lett.* **125**, 156801 (2020).
- [7] A. Fert, Nobel Lecture: Origin, development, and future of spintronics, *Rev. Mod. Phys.* **80**, 1517 (2008).
- [8] S. D. Bader and S. S. P. Parkin, Spintronics, *Annu. Rev. Condens. Matter Phys.* **1**, 71 (2010).
- [9] M. Kroutvar, Y. Ducommun, D. Heiss, M. Bichler, D. Schuh, G. Abstreiter, and J. J. Finley, Optically programmable electron spin memory using semiconductor quantum dots, *Nature (London)* **432**, 81 (2004).
- [10] T. S. Shamirzaev, Type-I semiconductor heterostructures with an indirect gap conduction band, *Semiconductors* **45**, 96 (2011).
- [11] D. S. Abramkin and T. S. Shamirzaev, Type-I indirect-gap semiconductor heterostructures on (110) substrates, *Semiconductors* **53**, 703 (2019).
- [12] M. E. Pistol, and C. E. Pryor, Band structure of segmented semiconductor nanowires, *Phys. Rev. B* **80**, 035316 (2009).
- [13] A. V. Khaetskii and Y. V. Nazarov, Spin relaxation in semiconductor quantum dots, *Phys. Rev. B* **61**, 12639 (2000).
- [14] A. V. Khaetskii and Y. V. Nazarov, Spin-flip transitions between Zeeman sublevels in semiconductor quantum dots, *Phys. Rev. B* **64**, 125316 (2001).
- [15] M. M. Glazov, *Electron & Nuclear Spin Dynamics in Semiconductor Nanostructures* (Oxford University Press, Oxford, 2018).
- [16] T. S. Shamirzaev, D. S. Abramkin, A. K. Gutakovskii, and M. A. Putyato, High quality relaxed GaAs quantum dots in GaP matrix, *Appl. Phys. Lett.* **97**, 023108 (2010).
- [17] D. S. Abramkin, M. A. Putyato, S. A. Budenny, A. K. Gutakovskii, B. R. Semyagin, V. V. Preobrazhenskii, O. F. Kolomys, V. V. Strelchuk, and T. S. Shamirzaev, Atomic structure and energy spectrum of Ga(As, P)/GaP heterostructures, *J. Appl. Phys.* **112**, 083713 (2012).
- [18] T. S. Shamirzaev, A. M. Gilinsky, A. K. Kalagin, A. V. Nenashev, and K. S. Zhuravlev, Energy spectrum and structure of thin pseudomorphic InAs quantum wells in an AlAs matrix: Photoluminescence spectra and band-structure calculations, *Phys. Rev. B* **76**, 155309 (2007).
- [19] D. S. Abramkin, K. M. Rumynin, A. K. Bakarov, D. A. Kolotovkina, A. K. Gutakovskii, and T. S. Shamirzaev, Quantum dots formed in InSb/AlAs and AlSb/AlAs heterostructures, *JETP Lett.* **103**, 692 (2016).
- [20] E. L. Ivchenko, Magnetic circular polarization of exciton photoluminescence, *Phys. Solid State* **60**, 1514 (2018).
- [21] T. S. Shamirzaev, J. Debus, D. R. Yakovlev, M. M. Glazov, E. L. Ivchenko, and M. Bayer, Dynamics of exciton recombination in strong magnetic fields in ultrathin GaAs/AlAs quantum wells with indirect band gap and type-II band alignment, *Phys. Rev. B* **94**, 045411 (2016).
- [22] T. S. Shamirzaev, J. Rautert, D. R. Yakovlev, J. Debus, A. Y. Gornov, M. M. Glazov, E. L. Ivchenko, and M. Bayer, Spin dynamics and magnetic field induced polarization of excitons in ultrathin GaAs/AlAs quantum wells with indirect band gap and type-II band alignment, *Phys. Rev. B* **96**, 035302 (2017).
- [23] T. S. Shamirzaev, Exciton recombination and spin dynamics in indirect-gap quantum wells and quantum dots, *Phys. Solid State* **60**, 1554 (2018).
- [24] T. S. Shamirzaev, J. Rautert, D. R. Yakovlev, and M. Bayer, Exciton recombination and spin relaxation in strong magnetic fields in ultrathin (In, Al)As/AlAs quantum wells with indirect band gap and type-I band alignment, *Phys. Rev. B* **104**, 045305 (2021).
- [25] T. S. Shamirzaev, D. R. Yakovlev, A. K. Bakarov, N. E. Kopteva, D. Kudlacik, A. K. Gutakovskii, and M. Bayer, Recombination and spin dynamics of excitons in thin (Ga, Al)(Sb, As)/AlAs quantum wells with an indirect band gap and type-I band alignment, *Phys. Rev. B* **102**, 165423 (2020).
- [26] T. S. Shamirzaev, J. Rautert, D. R. Yakovlev, M. M. Glazov, and M. Bayer, Intrinsic and magnetic-field-induced linear polarization of excitons in ultrathin indirect-gap type-II GaAs/AlAs quantum wells, *Phys. Rev. B* **99**, 155301 (2019).
- [27] T. S. Shamirzaev, J. Debus, D. S. Abramkin, D. Dunker, D. R. Yakovlev, D. V. Dmitriev, A. K. Gutakovskii, L. S. Braginsky, K. S. Zhuravlev, and M. Bayer, Exciton recombination dynamics in an ensemble of (In, Al)As/AlAs quantum dots with indirect band-gap and type-I band alignment, *Phys. Rev. B* **84**, 155318 (2011).
- [28] D. Keller, D. R. Yakovlev, B. König, W. Ossau, T. Gruber, A. Waag, L. W. Molenkamp, and A. V. Scherbakov, Heating of the magnetic ion system in (Zn, Mn)Se/(Zn, Be)Se semimagnetic quantum wells by means of photoexcitation, *Phys. Rev. B* **65**, 035313 (2001).
- [29] N. Shtinkov, P. Desjardins, R. A. Masu, and S. J. Vlaev, Lateral confinement and band mixing in ultrathin semiconductor quantum wells with steplike interfaces, *Phys. Rev. B* **70**, 155302 (2004).
- [30] P. Offermans, P. M. Koenraad, R. Notzel, J. H. Wolter, and K. Pierz, Formation of InAs wetting layers studied by cross-sectional scanning tunneling microscopy, *Appl. Phys. Lett.* **87**, 111903 (2005).
- [31] D. S. Abramkin, A. K. Gutakovskii, and T. S. Shamirzaev, Heterostructures with diffused interfaces: Luminescent technique for ascertainment of band alignment type, *J. Appl. Phys.* **123**, 115701 (2018).
- [32] M. Schowalter, A. Rosenauer, D. Gerthsen, M. Arzberger, M. Bichler, and G. Abstreiter, Investigation of In segregation in InAs/AlAs quantum-well structures, *Appl. Phys. Lett.* **79**, 4426 (2001).
- [33] R. Kaspi and K. R. Evans, Sb-surface segregation and the control of compositional abruptness at the GaAsSb/GaAs interface, *J. Cryst. Growth* **175-176**, Part 2, 838 (1997).
- [34] S. J. C. Mauger, M. Bozkurt, P. M. Koenraad, Y. Zhao, H. Folliot, and N. Bertru, An atomic scale study of surface termination and digital alloy growth in InGaAs/AlAsSb multi-quantum wells, *J. Phys.: Condens. Matter* **28**, 284002 (2016).
- [35] M. Losurdo, P. Capezzuto, G. Bruno, A. S. Brown, T. Brown, and G. May, Fundamental reactions controlling anion exchange

- during mixed anion heterojunction formation: Chemistry of As-for-Sb and Sb-for-As exchange reactions, *J. Appl. Phys.* **100**, 013531 (2006).
- [36] M. Schowalter, A. Rosenauer, D. Gerthsen, M. Grau, and M.-C. Amann, Quantitative measurement of the influence of growth interruptions on the Sb distribution of GaSb/GaAs quantum wells by transmission electron microscopy, *Appl. Phys. Lett.* **83**, 3123 (2003).
- [37] K. Muraki, S. Fukatsu, Y. Shiraki, and R. Ito, Surface segregation of In atoms during molecular beam epitaxy and its influence on the energy levels in InGaAs/GaAs quantum wells, *Appl. Phys. Lett.* **61**, 557 (1992).
- [38] M. A. Herman, D. Bimberg, and J. Christen, Heterointerfaces in quantum wells and epitaxial growth processes: Evaluation by luminescence techniques, *J. Appl. Phys.* **70**, R1 (1991).
- [39] D. C. Reynolds, D. C. Look, B. Jogai, R. Kaspi, K. R. Evans, and M. Estes, High quality interfaces in GaAs-AlAs quantum wells determined from high resolution photoluminescence, *J. Vac. Sci. Technol. B* **15**, 1703 (1997).
- [40] D. S. Abramkin, A. K. Bakarov, A. K. Gutakovskii, and T. S. Shamirzaev, Spinodal decomposition in InSb/AlAs heterostructures, *Semiconductors* **52**, 1392 (2018).
- [41] J. F. Heffernan, J. Hegarty, and R. Planel, Monolayer islands in an interrupted-growth type-II single quantum well, *Phys. Rev. B* **52**, 7818 (1995).
- [42] T. S. Shamirzaev, D. S. Abramkin, A. K. Gutakovskii, and M. A. Putyato, Novel self-assembled quantum dots in the GaSb/AlAs Heterosystem, *JETP Lett.* **95**, 534 (2012).
- [43] D. S. Abramkin, A. K. Bakarov, M. A. Putyato, E. A. Emelyanov, D. A. Kolotovkina, A. K. Gutakovskii, and T. S. Shamirzaev, Formation of low-dimensional structures in InSb/AlAs heterosystem, *Semiconductors* **51**, 1233 (2017).
- [44] I. N. Krivorotov, T. Chang, G. D. Gilliland, L. P. Fu, K. K. Bajaj, and D. J. Wolford, Exciton transport and nonradiative decay in semiconductor nanostructures, *Phys. Rev. B* **58**, 10687 (1998).
- [45] T. S. Shamirzaev, A. M. Gilinsky, A. K. Kalagin, A. I. Toropov, A. K. Gutakovskii, and K. S. Zhuravlev, Strong sensitivity of photoluminescence of InAs/AlAs quantum dots to defects: evidence for lateral inter-dot transport, *Semicond. Sci. Technol.* **21**, 527 (2006).
- [46] T. S. Shamirzaev, D. S. Abramkin, A. V. Nenashev, K. S. Zhuravlev, F. Trojanek, B. Dzurnak, and P. Maly, Carrier dynamics in InAs/AlAs quantum dots: Lack in carrier transfer from wetting layer to quantum dots, *Nanotechnology* **21**, 155703 (2010).
- [47] I. Vurgaftman, J. R. Meyer, and L. R. Ram-Mohan, Band parameters for III-V compound semiconductors and their alloys, *J. Appl. Phys.* **89**, 5815 (2001).
- [48] C. G. Van de Walle, Band lineups and deformation potentials in the model-solid theory, *Phys. Rev. B* **39**, 1871 (1989).
- [49] J. Debus, T. S. Shamirzaev, D. Dunker, V. F. Sapega, E. L. Ivchenko, D. R. Yakovlev, A. I. Toropov, and M. Bayer, Spin-flip Raman scattering of the Γ -X mixed exciton in indirect band gap (In, Al)As/AlAs quantum dots, *Phys. Rev. B* **90**, 125431 (2014).
- [50] V. Y. Ivanov, T. S. Shamirzaev, D. R. Yakovlev, A. K. Gutakovskii, Ł. Owczarczyk, and M. Bayer, Optically detected magnetic resonance of photoexcited electrons in (In, Al)As/AlAs quantum dots with indirect band gap and type-I band alignment, *Phys. Rev. B* **97**, 245306 (2018).
- [51] V. Y. Ivanov, D. O. Tolmachev, T. S. Shamirzaev, D. R. Yakovlev, T. Ślupinski, and M. Bayer, Optically detected magnetic resonance of indirect excitons in an ensemble of (In, Al, Ga)As/(Al, Ga)As quantum dots, *Phys. Rev. B* **104**, 195306 (2021).
- [52] R. I. Dzhiyev, V. L. Korenev, B. P. Zakharchenya, D. Gammon, A. S. Bracker, J. G. Tischler, and D. S. Katzer, Optical orientation and the Hanle effect of neutral and negatively charged excitons in GaAs/Al_xGa_{1-x} quantum wells, *Phys. Rev. B* **66**, 153409 (2002).
- [53] E. L. Ivchenko, *Optical Spectroscopy of Semiconductor Nanostructures* (Alpha Science, Harrow UK, 2005).
- [54] G. Bartsch, M. Gerbracht, D. R. Yakovlev, J. H. Blokland, P. C. M. Christianen, E. A. Zhukov, A. B. Dzyubenko, G. Karczewski, T. Wojtowicz, J. Kossut, J. C. Maan, and M. Bayer, Positively versus negatively charged excitons: A high magnetic field study of CdTe/Cd_{1-x}Mg_xTe quantum wells, *Phys. Rev. B* **83**, 235317 (2011).
- [55] D. Dunker, T. S. Shamirzaev, J. Debus, D. R. Yakovlev, K. S. Zhuravlev, and M. Bayer, Spin relaxation of negatively charged excitons in (In, Al)As/AlAs quantum dots with indirect band gap and type-I band alignment, *Appl. Phys. Lett.* **101**, 142108 (2012).